Solar Physics
DOI: 10.1007/●●●●●-●●●-●●●-●●●●-●

Prominence and Filament Eruptions Observed by the Solar Dynamics Observatory: Statistical Properties, Kinematics, and Online Catalog

P. I. McCauley[1] · Y. Su[2,1] · N. Schanche[1] · K. E. Evans[3,1] · C. Su[4,2] · S. McKillop[1] · K. K. Reeves[1]

© Springer ●●●●

arXiv:1505.02090v1 [astro-ph.SR] 8 May 2015

Abstract

We present a statistical study of prominence and filament eruptions observed by the Atmospheric Imaging Assembly (AIA) aboard the Solar Dynamics Observatory (SDO). Several properties are recorded for 904 events that were culled from the Heliophysics Event Knowledgebase (HEK) and incorporated into an online catalog for general use. These characteristics include the filament and eruption type, eruption symmetry and direction, apparent twisting and writhing motions, and the presence of vertical threads and coronal cavities. Associated flares and white-light coronal mass ejections (CME) are also recorded. Total rates are given for each property along with how they differ among filament types. We also examine the kinematics of 106 limb events to characterize the distinct slow- and fast-rise phases often exhibited by filament eruptions. The average fast-rise onset height, slow-rise duration, slow-rise velocity, maximum field-of-view (FOV) velocity, and maximum FOV acceleration are 83 Mm, 4.4 hours, 2.1 km s^{-1}, 106 km s^{-1}, and 111 m s^{-2}, respectively. All parameters exhibit lognormal probability distributions similar to that of CME speeds. A positive correlation between latitude and fast-rise onset height is found, which we attribute to a corresponding negative correlation in the average vertical magnetic field gradient, or decay index, estimated from potential field source surface (PFSS) extrapolations. We also find the decay index at the fast-rise onset point to be 1.1 on average, consistent with the critical instability threshold theorized for straight current channels. Finally, we explore

✉ P. I. McCauley
pmccauley@cfa.harvard.edu

✉ Y. Su
ynsu@pmo.ac.cn

[1] Harvard-Smithsonian Center for Astrophysics, Cambridge, MA 02138, USA

[2] Key Laboratory for Dark Matter and Space Science, Purple Mountain Observatory, Chinese Academy of Sciences, Nanjing 210008, China

[3] Department of Astronomy, University of Maryland, College Park, MD 20742, USA

[4] School of Astronomy and Space Science, Nanjing University, Nanjing 210093, China

relationships between the derived kinematics properties and apparent twisting motions. We find that events with evident twist have significantly faster CME speeds and significantly lower fast-rise onset heights, suggesting relationships between these values and flux rope helicity.

Keywords: Prominences, Dynamics; Coronal Mass Ejections, Low Corona Signatures; Corona, Structures

1. Introduction

Prominences are among the most common and well-studied features of the solar atmosphere, having been chronicled since the Middle Ages and identified as "cloud formations" in the corona in the 1850s (Tandberg-Hanssen, 1998). They are now recognized to be thin channels of relatively cool, dense plasma suspended in the corona by highly sheared or twisted magnetic fields above polarity inversion lines in the photospheric magnetic flux distribution. Bright in Hα emission when protruding from the limb, prominences appear dark compared to the surrounding chromosphere when seen on the disk, where they are referred to as filaments. We will use the terms *prominence* and *filament* interchangeably. Readers seeking detailed background information may direct their attention to the recent book, *Solar Prominences* (Vial and Engvold, 2015), from which we reference several chapters, and the excellent review of prominence observations by Parenti (2014).

This paper focuses on prominence eruptions observed by the Atmospheric Imaging Assembly (AIA, Lemen *et al.* 2012) aboard the Solar Dynamics Observatory (SDO, Pesnell, Thompson, and Chamberlin 2012), launched in 2010. The AIA provides continuous, full-sun coverage in 7 extreme ultraviolet (EUV) and 3 UV channels with high time (12s) and spatial (0.6″) resolution. A number of case studies have been published on AIA observations of eruptive prominences. Sterling, Moore, and Freeland (2011), Tripathi *et al.* (2013), and Chen, Bastian, and Gary (2014) present separate observations of active region filament eruptions, each found to be consistent with an erupting flux-rope model. Su and van Ballegooijen (2012, 2013) present observations and flux-rope modeling of a polar crown eruption, and Thompson (2013) further examines signs of twist in the same event. Williams, Baker, and van Driel-Gesztelyi (2013) estimate the mass of erupted filament material in a particularly stunning event, and several authors have combined the SDO with the Solar Terrestrial Relations Observatory (STEREO, Howard *et al.* 2008) spacecraft to examine prominence eruptions from three separate viewing angles (e.g. Chifu *et al.* 2012; Koleva *et al.* 2012). Su, Lu, and van Ballegooijen (2012) present a survey of 45 quiescent prominence eruptions observed by the SDO that serves as a pilot study for our work, with results generally consistent with those to be described here.

We have recorded some basic observational properties for 904 filament eruptions observed by the AIA, compiled an online catalog designed to aid the community in identifying promising events for future research, and performed a kinematics study using events selected from the catalog. §2 describes the catalog and the observations it provides. §3 details the recorded properties, including some background information on their significance and a report of our results. These include the filament type (§3.1), eruption symmetry (§3.2) and direction (§3.3), apparent twisting (§3.4) and writhing (§3.5) motions, the presence of vertical threads (§3.6) and coronal cavities (§3.7), and white-light CME (§3.8) associations. §4 details our kinematics study. This involves height-time measurements of 106 limb eruptions, which are fit with an analytic approximation to provide statistics on the slow- and

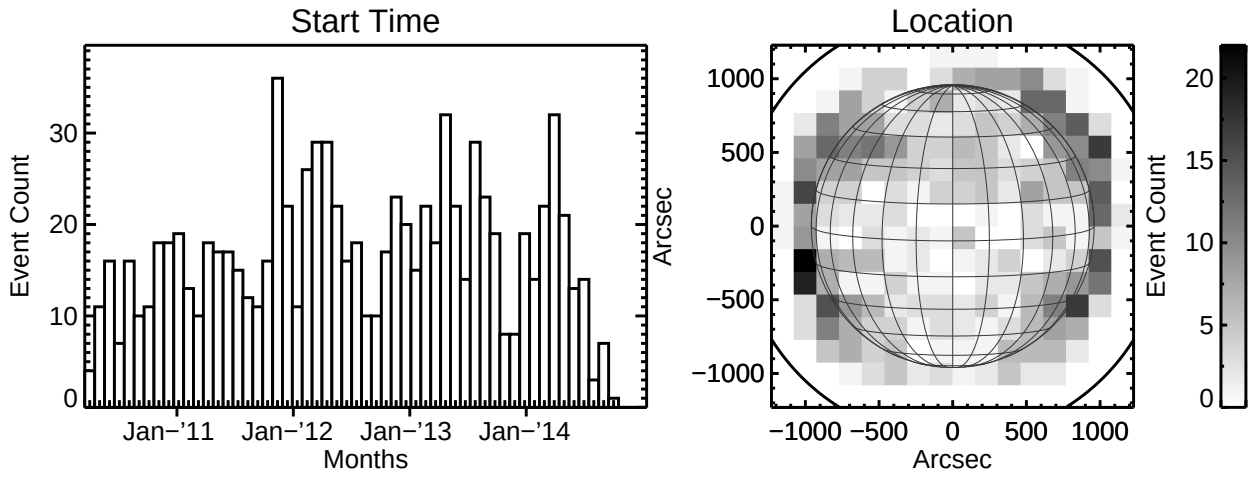


Figure 1. Start time (left) and position (right) data for filament eruptions found in the HEK and incorporated in the catalog.

fast-rise phases often exhibited by filament eruptions. Our methods are detailed in §4.1, the analytic approximation is described in §4.2, the impact of solar rotation is considered in §4.3, and our results are described in §4.4. §5 discusses interesting patterns that emerge, including a correlation between latitude and the fast-rise onset height (§5.1) along with suggestive relationships between apparent twisting motions and the derived kinematics values (§5.2). Finally, §6 summarizes our work.

2. Online Catalog

The catalog includes 904 filament eruptions observed by the SDO between June of 2010 and September of 2014. Times and positions are obtained from the Heliophysics Event Knowledgebase[1] (HEK, Hurlburt *et al.* 2012), which incorporates a wide variety of phenomena and relies on reports from individual observers for filament eruptions. Figure 1 shows the event time and position distributions. An enhancement of eruptions near the limb is apparent, which is primarily due to the contribution of events behind the limb. We also note the general position of each eruption, finding 401 disk events, 363 limb events, and 139 events originating behind the limb.

For each event, we provide cutout and full-disk movies in the 171, 193, and 304 Å AIA passbands. If available, full-disk observations are also provided from the 304 Å channels of the Extreme Ultraviolet Imagers (EUVI, Wuelser *et al.* 2004) aboard the STEREO spacecraft. Images are obtained primarily from the Helioviewer[2] application program interface (API), which provides full-resolution JPEG2000 images that we then process separately to produce our content. In most cases, the 171 Å images are processed from the original level 1 data files using a radial filter described by Masson *et al.* (2014). All movies are provided for download and may also be played via YouTube.

Users may sort and filter the catalog based on the characteristics described in §3. Additional comments on each event from the HEK and catalog observers are also provided and may be used to search the catalog for specific terms. Further details on the interface

[1]Heliophysics Event Knowledgebase: http://www.lmsal.com/hek/

[2]Helioviewer: http://helioviewer.org/

can be found at the catalog website[3]. Each event is also assigned an arbitrary rating based on how interesting a particular observer found it to be, which is intended to aid users who wish to browse through the large number of eruptions. A collection of movies from the highest-rated events is available as a YouTube playlist or as a downloadable TAR file, which may also be useful for education and public outreach. The catalog table may also be downloaded as an IDL save file or as a tab-delimited text file. Finally, we note that the structure of the website is essentially the same as that of the Hinode/XRT Flare Catalog[4] and the Hinode & SDO Sigmoid Catalog[5] (Savcheva *et al.*, 2014).

3. Statistical Properties

The following subsections detail the properties recorded for each event, including brief background information on their significance and a report of our results. Each determination was made through manual inspection by one of three observers with the exception of flare associations, which are automatically populated using data from the "Latest Events" archive in SolarSoft[6] and are not discussed further. Table 1 lists the event counts for each category, while Figures 2-9 provide representative examples and bar plots of the category distributions. All images are single frames from the event movies provided in the catalog with no additional processing. Clicking the ID numbers listed in the electronic text (e.g. No. 0962) will launch the catalog website, where the associated movies can be found.

3.1. Type

We assign types based on the commonly-used, location-based scheme. *Active region* (AR) filaments are found within active regions, *intermediate* prominences (IP) are found adjacent to or between active regions, *quiescent* (QS) filaments are found well away from active regions in the quiet sun, and *polar crown* (PC) prominences are found at high latitudes. Figure 2 shows representative examples of each type. Note that PC may refer specifically to filaments that form at the boundaries of the polar coronal holes, but we use the term more generally to refer to any filament with a latitude greater than $\sim 50^\circ$ N/S. Including ambiguous events (e.g. "AR?"), our sample includes 172 AR, 124 IP, 451 QS, and 132 PC filament eruptions. An additional 20 eruptions are of indeterminable type. These events are generally behind the limb without available STEREO observations, though a few are very compact filaments in small emerging flux regions that do not fit neatly into the four main groups. 5 more are classified as *transequatorial* (TE) filaments, the longest and rarest variety. Neither of these latter two groups are included in the discussions below, but we find that the TE events have characteristics most similar to QS eruptions. Other classification schemes exist based on morphology, dynamics, spectroscopic characteristics, and magnetic configuration. A review of these, along with historical classifications, is provided by Engvold (2015). It would be worthwhile to investigate a subset of the events and characteristics described below using additional type sets, particularly the scheme based on photospheric flux distribution advanced by Mackay, Gaizauskas, and Yeates (2008).

The extent to which each filament erupts is also categorized, guided by conventions described by Gilbert, Alexander, and Liu (2007). A *full* (F) eruption is one in which

[3]SDO Filament Eruption Catalog: http://aia.cfa.harvard.edu/filament/
[4]Hinode/XRT Flare Catalog: http://xrt.cfa.harvard.edu/flare_catalog/
[5]Hinode & SDO Sigmoid Catalog: http://aia.cfa.harvard.edu/sigmoid/
[6]SolarSoft Latest Events: http://www.lmsal.com/solarsoft/latest_events/

Table 1. Properties and event counts. Ambiguous (e.g. "Y?") event counts are listed in parens.

Category	Bin	Type						
		All	AR	IP	QS	PC	TE	?
Type		904	135 (37)	76 (48)	392 (59)	122 (10)	4 (1)	20
Position	Disk	401	92	68	214	19	5	3
	Limb	363	50	48	178	82	0	5
	Behind	139	30	8	58	31	0	12
Eruption	Full	285 (73)	56 (13)	39 (7)	143 (42)	36 (9)	3	8 (2)
	Partial	266 (99)	38 (23)	38 (17)	131 (49)	53 (7)	2	4 (3)
	Confined	122 (56)	33 (9)	15 (7)	57 (29)	14 (11)	0	3 (0)
	Other[a]	18 (2)	5 (1)	1	10 (1)	2	0	0
Symmetry	Sym	307 (126)	41 (30)	49 (13)	174 (62)	34 (17)	2 (1)	7 (3)
	Asym	232 (114)	49 (19)	29 (16)	116 (48)	33 (27)	1 (1)	4 (3)
	?	125	33	17	51	21	0	3
Direction	Radial	625 (51)	95 (12)	79 (3)	338 (26)	97 (7)	2 (2)	14 (1)
	Non-R	73 (35)	11 (6)	12 (4)	39 (17)	10 (6)	0	1 (2)
	Sideways	72 (26)	36 (8)	18 (5)	12 (8)	5 (4)	1	0 (1)
	?	22	4	3	11	3	0	1
Twist	Yes	408 (130)	70 (31)	65 (19)	201 (63)	58 (14)	1	13 (3)
	No	265 (68)	44 (14)	28 (8)	143 (34)	47 (10)	1 (1)	2 (1)
	?	32	13	4	9	3	2	1
Writhe	Yes	73 (71)	26 (14)	15 (10)	27 (38)	1 (7)	0	4 (2)
	No	656 (61)	102 (14)	79 (13)	350 (23)	110 (10)	5	10 (1)
	?	43	16	7	13	4	0	3
Vertical Threads[b]	Yes	384 (58)	10 (6)	52 (16)	246 (30)	69 (6)	4	3
	No	296 (26)	118 (8)	42 (6)	105 (11)	26	0 (1)	5
Cavity[c]	Yes	97 (27)	2 (2)	10	47 (12)	37 (12)	0	1 (0)
	No	165 (13)	35	25	79 (8)	25 (5)	0	1
	During	47 (14)	9 (2)	9 (3)	24 (8)	3	0	2 (1)
CME	Yes	609 (44)	108 (12)	85 (8)	307 (18)	91 (5)	4	14 (1)
	No	225 (26)	50 (2)	26 (5)	112 (14)	32 (4)	1	4 (1)
Flare	Yes	222 (15)	94 (2)	50 (3)	68 (9)	7 (1)	1	2
	No	682 (15)	78 (2)	74 (3)	383 (9)	125 (1)	4	18

[a]Indicates non-eruptive events that are excluded from all other counts.
[b]Vertical threads counts exclude events behind the limb.
[c]Cavity counts include limb events only.

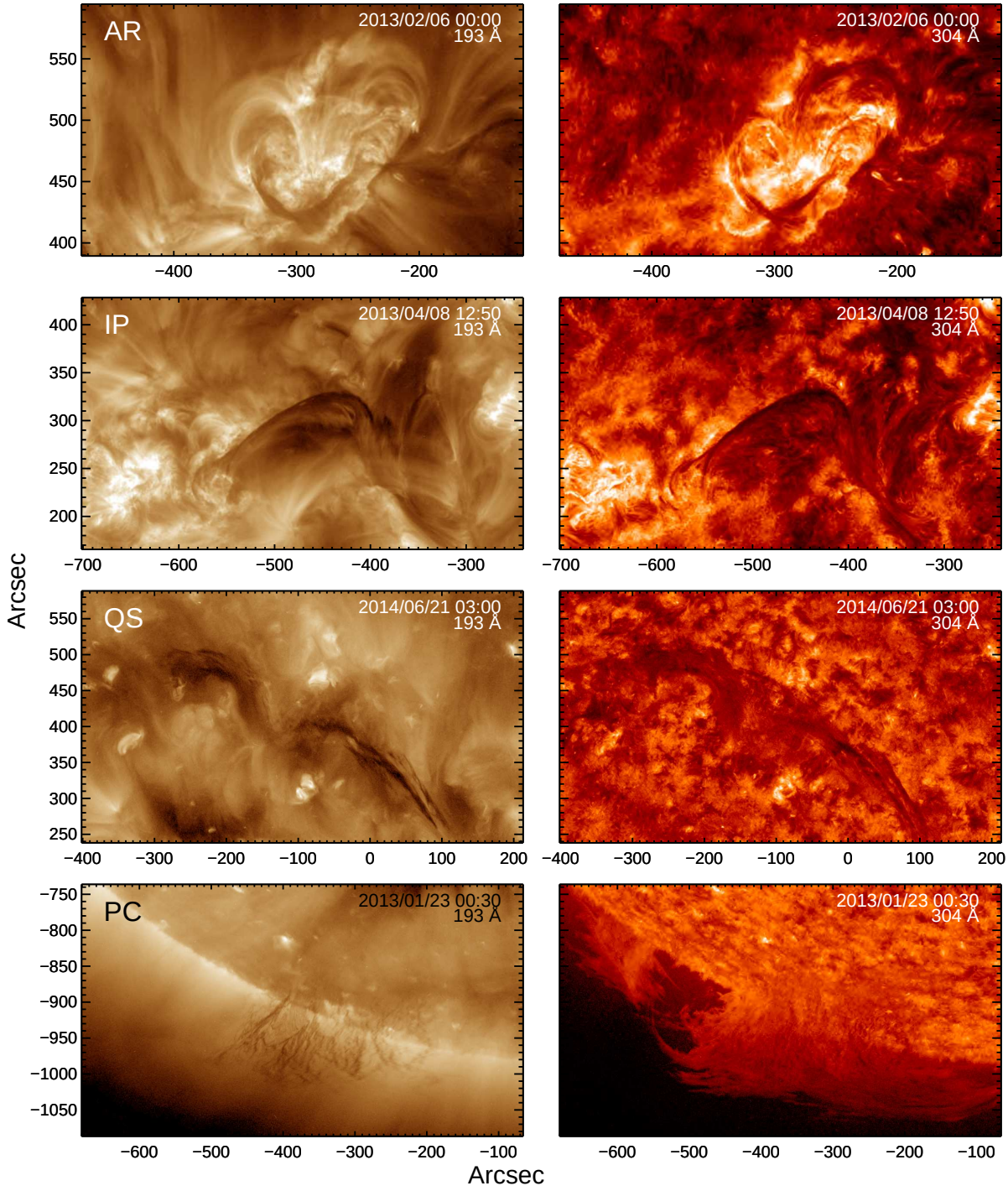


Figure 2. Examples of the four main types: active region (AR, No. 0631), intermediate (IP, No. 0667), quiescent (QS, No. 0977), and polar crown (PC, No. 0621).

the bulk of the filament mass escapes the AIA field-of-view (FOV) along with the full magnetic structure, a *partial* (P) eruption is one in which the magnetic structure erupts either completely or partially, expelling some or none of the filament mass, and a *confined* (C) or failed eruption is one in which none of the filament mass nor magnetic structure escapes. It can be difficult in practice to apply these straightforward definitions because all events exhibit some draining, whereby expelled material flows back down the legs of an erupting prominence. This returned mass may constitute an apparently significant

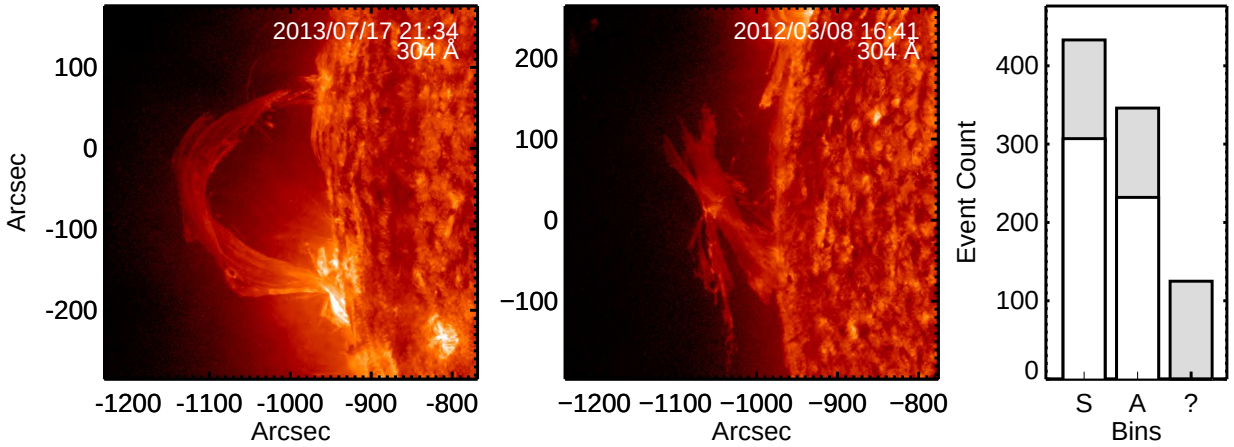


Figure 3. Examples of symmetric (left, No. 0745) and asymmetric (middle, No. 0405) eruptions. The right panel shows the number of events found for each type, and shaded regions denote ambiguous events (e.g. "S?").

volumetric fraction of the material seen, but it is not necessarily clear what fraction of the actual mass escapes given that the volume of the structure is evolving and that the 304 Å observations we primarily rely on are optically thick even at low column densities. For this reason, we relax the >90% criterion used by Gilbert, Alexander, and Liu (2007) and define a full eruption as one in which the magnetic structure erupts completely and no more than a third of the filament material appears to drain back down. Question marks are used to denote events near this boundary.

It can also be difficult to make a determination for faint events that become too diffuse to be tracked to the edge of the FOV or distinguished from the background chromosphere on the disk; these are labeled as full if they appeared to be erupting fully prior to becoming untraceable. The very few instances in which a filament channel erupts with little or no filament material contained within it are labeled as partial eruptions (e.g. No. 0478). Finally, note that these labels are of course based on the behavior of the filament and associated magnetic structure to the extent to which they are visible in the three passbands we examine. It may be possible, for instance, for an apparently confined event to produce a detectable CME either because an eruption was stimulated in the overlying field or because some part of the prominence structure escaped without producing a noticeable signature in our observations (see §3.8). Given these definitions and including ambiguous events (e.g. F?), the catalog includes 358 full, 365 partial, and 178 confined eruptions. An additional 20 events are labeled as *other* (O), which include non-eruptive dynamics such as filament activation. These events are included in the online catalog but are excluded from all counts in this paper.

3.2. Symmetry

Filament eruptions are often divided into symmetric and asymmetric categories depending on whether they exhibit a loop-like geometry or one that favors the liftoff of a single footpoint. This distinction is particularly useful for studies of potential eruption mechanisms and magnetic configurations. For instance, Tripathi, Isobe, and Mason (2006) examined EUV brightenings associated with both types and found that in the symmetric case, brightenings propagated from the middle to each end, while in the asymmetric case, they moved from the erupting end toward the tethered one. Based on this, they suggest a three-dimensional extension to the standard two-dimensional flare model in which the EUV

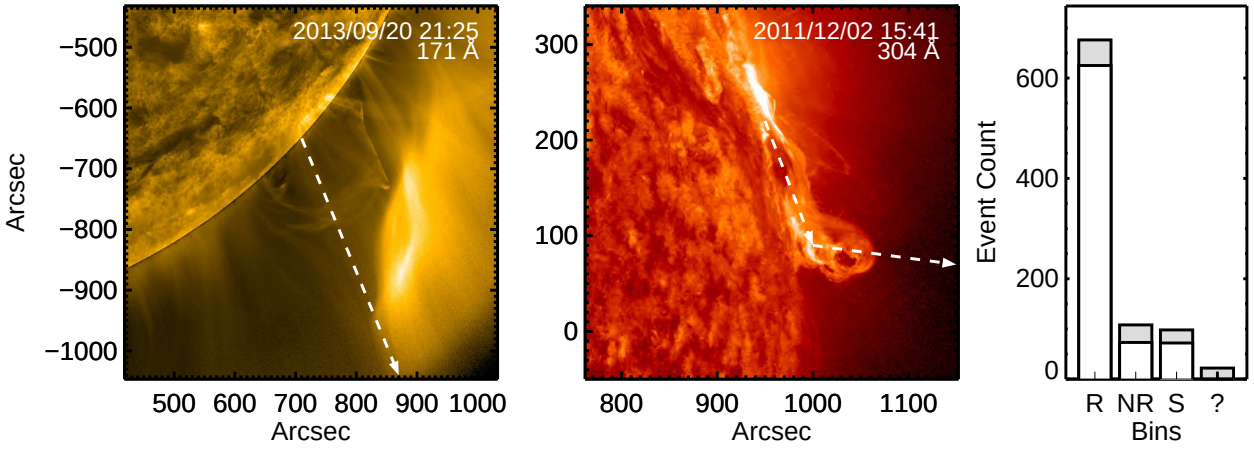


Figure 4. Examples of non-radial (left, No. 0797) and sideways (middle, No. 0332) trajectories. Arrows denote the approximate trajectories. The right panel shows the total number of radial (R), sideways (S), and non-radial (NR) events, and the shaded regions denote ambiguous events (e.g. "NR?").

brightenings are caused by successive reconnection events. Liu, Alexander, and Gilbert (2009) further divided asymmetric events into "whipping" and "zipping" types for which the active leg either whips upward dramatically or moves along the polarity inversion line like the unfastening of a zipper, with each case exhibiting distinct hard X-ray patterns and implying different field configurations.

We distinguish simply between the *symmetric* (S) and *asymmetric* (A) cases based primarily on inspection of 304 Å observations. This distinction may be obscured by the orientation of the filament and its two-dimensional projection, such as when the filament has a predominantly east-west axis and is positioned on the limb. For this reason, there are a large number of ambiguous (e.g. "S?") and indeterminable ("?") events. Figure 3 provides examples of both cases along with a bar plot showing the frequency distribution. Including ambiguous events, we find that 48% of eruptions are symmetric, 38% are asymmetric, and 14% are indeterminable. The respective percentages of symmetric and asymmetric events by filament type are 41% and 40% for AR, 50% and 36% for IP, 52% and 36% for QS, and 39% and 45% for PC eruptions. Symmetric eruptions are thus somewhat more common for each type except polar crown filaments. It is possible that the longer length of PC filaments could provide more opportunities for one footpoint to be preferentially destabilized by neighboring events, however these differences may not be very significant given large number of questionable and indeterminable events. More significantly, symmetric events are around 1.5× more likely to be full eruptions than asymmetric ones. This is primarily because the asymmetric geometry allows mass to more easily drain out of the filament before it is fully expelled and because asymmetric events frequently leave behind a section of the filament at the end opposite to the initial liftoff.

3.3. Direction

The directions of filament eruptions and associated CMEs are influenced by the surrounding magnetic environment, which may deflect an eruption away from a simple radial trajectory. Such interactions between small- and large-scale magnetic structures are of particular interest in the space weather context because CME deflection influences an event's potential to impact Earth (Kay, Opher, and Evans, 2014). Gopalswamy (2015) provides a recent review of non-radial prominence trajectories, which generally match that of the associated white-light CMEs (Simnett, 2000) but often exhibit a greater degree

of non-radiality (Panasenco *et al.*, 2013). Eruptions will tend to travel along the paths of least resistance, deflecting away from regions of higher magnetic energy density (Gui *et al.*, 2011) such as coronal holes and active regions.

We distinguish between three types of trajectories: *radial* (R), *non-radial* (NR), and *sideways* (S). Non-radial events are somewhat inclined from a radial trajectory and are generally deflected by large scale features such as coronal holes and pseudo-streamers. Sideways events have a substantial tangential component initially and are generally deflected away from active regions, often adopting a radial trajectory while still within the AIA FOV. Figure 4 provides examples of the latter two cases along with a bar plot showing the category distributions. The non-radial example is deflected southward by an overlying pseudo-streamer and the sideways example is ejected tangentially out of its host AR. Including ambiguous events (e.g. "NR?"), we find that 75% of eruptions are radial, 12% are non-radial, 11% are sideways, and 2% are indeterminable. By type, the respective percentages of non-radial and sideways events are 10% and 26% for AR, 13% and 19% for IP, 12% and 4% for QS, and 12% and 7% for PC eruptions. Similar non-radial rates of around $12 \pm 1\%$ are found for full, partial, and confined eruptions. However, these groups exhibit sideways trajectories at different rates of 7%, 12%, and 16%, respectively. Sideways eruptions are more frequently confined or partial perhaps because they are more likely to encounter neighboring magnetic structures that might arrest the entire eruption or divert some ejecta along a different set of field lines. Alternatively, eruptions may be confined due to the prevailing strength of the overlying field and recorded as sideways if the material is diverted tangentially before draining back to the surface.

Future work on quantifying the extent to which eruptions deviate from the radial direction and on what prompts this deviation might start from the events identified here. In particular, there is at present no clearly-articulated model describing the evolution of the magnetic field in the sideways ejection events from ARs. One hypothesis is that such trajectories arise from configurations in which the overlying coronal arcade in the center of the active region is too strong for the flux rope to break through radially. Instead, the system may first destabilize in the weaker-field region at the active region periphery. This might explain why filament plasma is seen to move horizontally from strong to weak field regions at the start of some events. However, if the stronger-field side is suddenly diminished by flux cancellation or footpoint motions, the filament may also eject toward the weakened stronger-field side. Thus, new insights might be gleaned from magnetic field modeling along with a careful examination of potential changes in the photospheric flux distribution for some events in our sideways sample.

3.4. Twist

Apparent twist in filament eruptions is particularly intriguing because of its relationship to stored energy release and interactions with nearby magnetic structures. Several types of twist may be observed, each with different implications. For instance, the "roll effect" refers to rotation about the filament axis whereby the loop apex rolls to one side, creating twist of opposite signs in the two legs (Martin, 2003). Panasenco *et al.* (2011) explore this effect for three eruptions observed by STEREO, and Panasenco *et al.* (2013) consider its connection to prominence trajectories, showing a relationship between roll and the presence of large-scale features like coronal holes and pseudo-streamers that may induce rolling motions through deflection. Murphy *et al.* (2012) suggest that rolling may also arise from an offset between a rising flux rope and the corresponding CME current sheet.

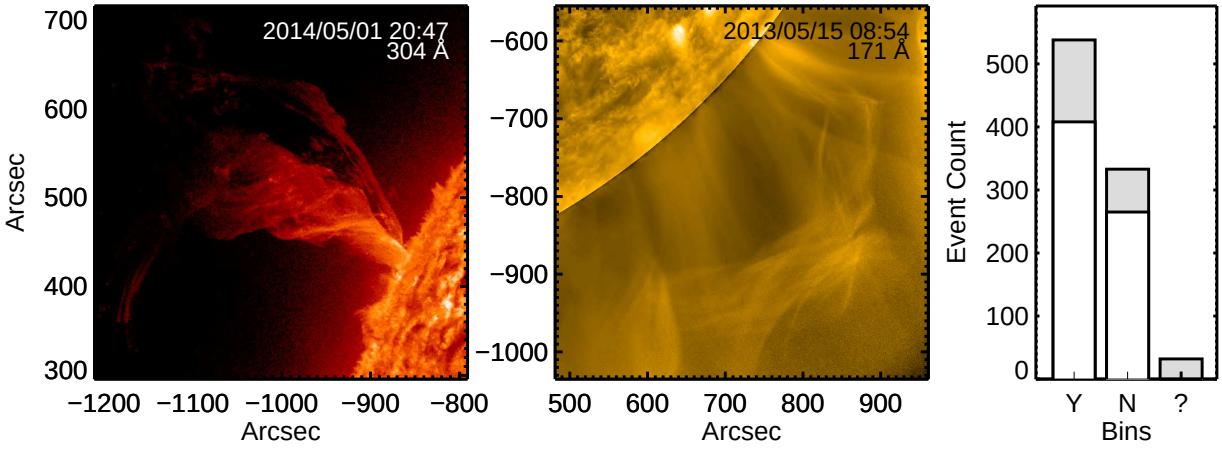


Figure 5. Examples of events exhibiting twist (left: No. 0994, right: No. 0696). The right panel shows the number of events that do (Y) and do not (N) show twist, and the shaded regions denote ambiguous events (e.g. "Y"?).

Su and van Ballegooijen (2013) model a PC eruption, reproducing rolling motions observed at low heights through a continuous injection of twist from the active region side that creates an asymmetric field distribution, possibly inducing rolling motions through asymmetric reconnection similar to that described by Murphy *et al.* (2012). Su and van Ballegooijen also describe further rotating motions attributed to the relaxing of dipped field lines after the eruption (see also Thompson 2013). Romano, Contarino, and Zuccarello (2003) explore untwisting motions in detail, which can often be seen in one or both legs during eruptions (e.g. Yan *et al.* 2014). Mass flow during an eruption may also reveal twisted structure inherent to the filament. Finally, a distinction can be drawn between *twist*, which generally refers to the degree to which field lines are wound around a central axis, and *writhe*, the helical deformation (twist) of the axis itself that may lead to the kink instability (Török, Berger, and Kliem, 2010). These properties may be combined into the mathematical measure *helicity*, which quantifies the degree to which a magnetic field is twisted, writhed, and linked. Helicity is positively related to free magnetic energy, and helicity accumulation is thought to be very important in leading to an eruption (Tziotziou *et al.*, 2014).

In this work, we assess simply whether (un)twisting motions of any type are apparent in each eruption, and references to "twisting motions" here and in later sections indicate the presence of at least one of the twist signatures described above. It was our initial intent to subdivide twist into categories related to the previous discussion, but we found that the careful inspection required to make these distinctions was untenable for our large sample and additional aims. Future work on this topic is planned, and some preliminary results were shown by McKillop *et al.* (2014). However, we do note that the untwisting motions in filament legs and mass flow that reveals twisted structure are the most commonly-observed of these phenomena in our events. Figure 5 shows two examples and the event count distribution. Including ambiguous events (e.g. "Y?"), we find that 60% of events show signs of twist, 37% do not, and the remainder are indeterminable. By type, the percentage of events with evident twist are 59% for AR, 68% for IP, 59% for QS, and 55% for PC eruptions. We therefore find that a majority of all filament types exhibit signs of twist and that the likelihood is highest for IP eruptions.

We also find that events with apparent twisting motions have faster CME speeds on average, and that IP events are generally the fastest of the four types (see §4.4 and

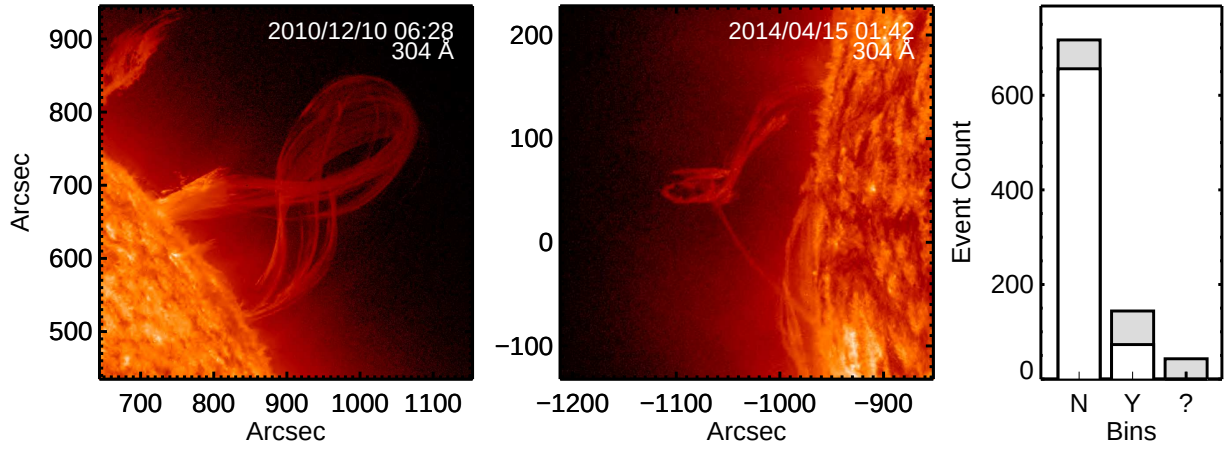


Figure 6. Examples of events exhibiting writhe (left: No. 0126, right: No. 0927). The right panel shows the number of events that do (Y) and do not (N) show writhing, and the shaded regions denote ambiguous events (e.g. "Y"?).

§5.2). Full and partial eruptions exhibit twisting motions at similar rates of 61% and 66%, respectively. Interestingly, confined eruptions are significantly less likely to exhibit signs of twist, with a rate of 44%, despite including a comparatively higher rate of events with writhing motions (see §3.5). We hypothesize that events exhibiting twisting motions will have had greater helicity on average, which implies a greater release of magnetic energy during the eruptions. The lower rate of twisting motions in confined events thus might be understood in terms of the energy available to push through the overlying field. Relationships between apparent twisting motions and eruption kinematics will be explored in §5.2.

3.5. Writhe

The helical kink instability is an ideal magnetohydrodynamic (MHD) instability that affects columns of plasma with strong axial currents, such as magnetic flux ropes, and is so named for the characteristic inverted gamma shape of kinked rope. As described in the previous section, the helical deformation of a flux rope's axis that may ultimately produce a kinked shape is generally referred to as *writhe* (Török, Berger, and Kliem, 2010). The kink instability is one of the principal mechanisms thought to drive prominence eruptions (see §5 and review by Fan 2015), and numerical simulations of kink-unstable flux ropes have been very successful in reproducing characteristics of observed events (Török and Kliem, 2005), suggesting that coronal flux ropes exist prior to eruption (Gibson and Fan, 2006). An overview of how the kink instability manifests in solar observations is given by Gilbert, Alexander, and Liu (2007), and a recent effort to quantify the twist in a likely kink-unstable event is presented by Yan *et al.* (2014).

We note the appearance of writhing based on inspection of the 304 and 171 Å observations. Figure 6 provides two examples along with a bar plot showing the distribution of events with and without. Including ambiguous events (e.g. "Y?"), we find that 79% of eruptions show no writhe, 16% do, and another 5% were indeterminable. However, fully half of the 144 writhed events are labeled as ambiguous. This is due to the difficulty in positively identifying the inverse-gamma structure, which may be obscured by the orientation or dynamics of the event. By type, we find that 23% of AR, 20% of IP, 14% of QS, and 6% of PC eruptions exhibit writhing motions. 62% and 23% of the writhed events are partial and confined eruptions, respectively, which are significantly greater than the general population

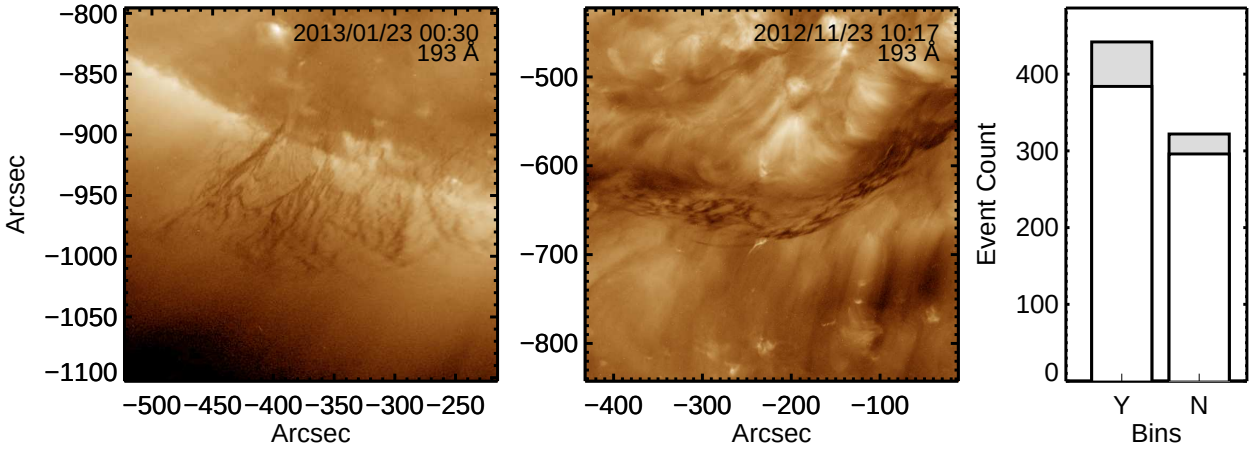


Figure 7. Examples of vertical absorption threads on the limb (left, No. 0578) and disk (middle, No. 0797). The right panel shows the number of events with (Y) and without (N) vertical threads, excluding events behind the limb, and the shaded regions denote ambiguous events (e.g. "Y?").

rates of 40% and 20%. This is consistent with expectations from Gilbert, Alexander, and Liu (2007), who note that kinking structures are highly unlikely to produce full eruptions because the filament material needs to be concentrated at the center of the flux rope and the eruption needs to be sufficiently fast to limit draining. We do find that 15% of our kinked sample (22 events) are full eruptions, which might be greater than expected by Gilbert, Alexander, and Liu. This is largely due to our comparatively lax definition of "full" (see §3.1), which permits more draining, however at least a few events exhibiting writhing motions appear to be full eruptions even with the stricter definition (e.g. No. 0770 & No. 0207). It is also important to note that a number of additional events classified as having apparent twisting motions in the previous section might also have been influenced by the kink instability but had underdeveloped or obscured inverse-gamma structures.

3.6. Vertical Threads

Thin threads, revealed primarily by high-resolution Hα imaging, are the ubiquitous building blocks of solar filaments (Lin, Martin, and Engvold, 2008). These are field-aligned and oriented horizontally, parallel or somewhat inclined with respect to filament spines and barbs. In addition to horizontal threads, vertical threads, perpendicular to the spine, are frequently observed in quiescent and polar crown "hedgerow" prominences (Engvold, 2015). Vertical threads are challenging to explain given the predominantly horizontal orientation of the local magnetic field (Paletou *et al.*, 2001), and several scenarios have been proposed. For instance, van Ballegooijen and Cranmer (2010) suggest that vertical threads form in a tangled field environment, Chae (2010) suggests that they form from stacks of sagging horizontal threads, and Low *et al.* (2012a,b) suggest that vertical structures may arise from cross-field mass transport after a breakdown of the frozen-in magnetic field condition, perhaps in concert with magneto-thermal convection as described by Berger *et al.* (2011).

We note the visibility of vertical threads (or more generally, threads perpendicular to the filament spine) based primarily on inspection of the 193 Å images. The threads appear dark in the EUV, as emission is absorbed and not produced by the neutral hydrogen and helium of the partially-ionized prominence plasma, which typically has HI column densities of $\sim 10^{19}$ cm^{-2} (Labrosse *et al.*, 2011). Figure 7 shows examples of vertical threads seen on the limb and on the disk, along with a bar plot showing the number of events with and without. Including the ambiguous events (e.g. "Y?"), and excluding those behind the

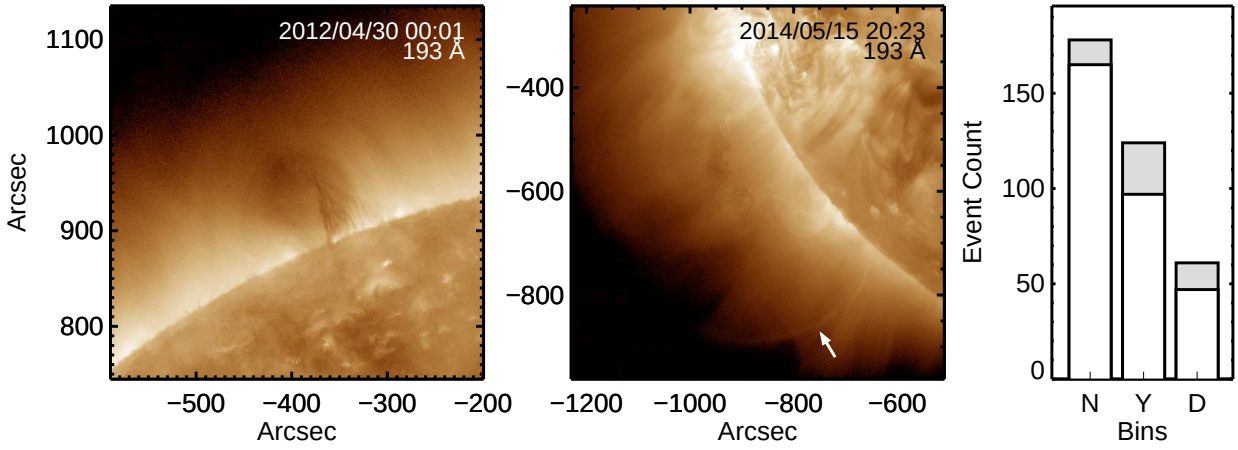


Figure 8. Examples of a coronal cavity (left, No. 0452) and a cavity that became apparent during the eruption (middle, see movie: No. 0953). The right panel shows the number of *limb* events with (Y), without (N), and during (D), and the shaded regions denote ambiguous events (e.g. "Y?").

limb, we find that 58% of events exhibit vertical threads and 42% do not. By type, the percentage of events with vertical threads are 11% for AR, 59% for IP, 70% for QS, and 74% for PC eruptions. The size of a filament influences whether the threads themselves or their orientations will be distinguishable, and we find rates that grow with the characteristic size scales of the four filament types. Confined events are also much less likely to exhibit vertical threads (43%), perhaps due to their generally smaller sizes. This may be caused by limited spatial resolution, or it may be that compact filaments are indeed less likely to contain vertical threads. We also note that the 16 AR events that do exhibit vertical threads are generally more extended, with higher pre-eruption heights, than average for that type. Several of these events are also on the boundary between what might be considered an "active region" versus "intermediate" filament or are found within decaying active regions with well-separated polarities. Thus, we find the presence of vertical threads to be the norm outside of active regions, and we note that our rates may be underestimated because some small or unfavorably-oriented filaments were likely excluded.

3.7. Cavity

Coronal cavities are elliptical depressions in the intensities above and surrounding prominences observed at optical, EUV, and soft X-ray wavelengths. They can be understood as the limb projections of filament channels on the disk, which may or may not contain a filament, and their interiors are less dense (Fuller and Gibson, 2009) and often hotter (Reeves *et al.*, 2012) than the surrounding plasma. Cavities are commonly modeled as magnetic flux ropes (e.g. Low and Hundhausen 1995; Fan 2012) and may be inherent components of filament systems that form from helicity accumulation (Mackay, 2015). At least a third of cavities erupt (Forland *et al.*, 2013), though many of those that do not may simply erupt sometime after they were observed at the limb. CMEs often exhibit a three-part structure that includes a bright plasma pileup followed by a dark cavity and bright prominence core (Hundhausen, 1999). A recent review of cavities is provided by Gibson (2015).

We note the visibility of associated cavities based on inspection of 193 Å observations, which are sensitive to material around 1.2 MK in non-flaring regions. Of the AIA passbands, cavities are most clearly delineated in this channel along with the 211 Å band, which is not included in the catalog. *No* (N) indicates that a cavity was not apparent, *yes* (Y) indicates

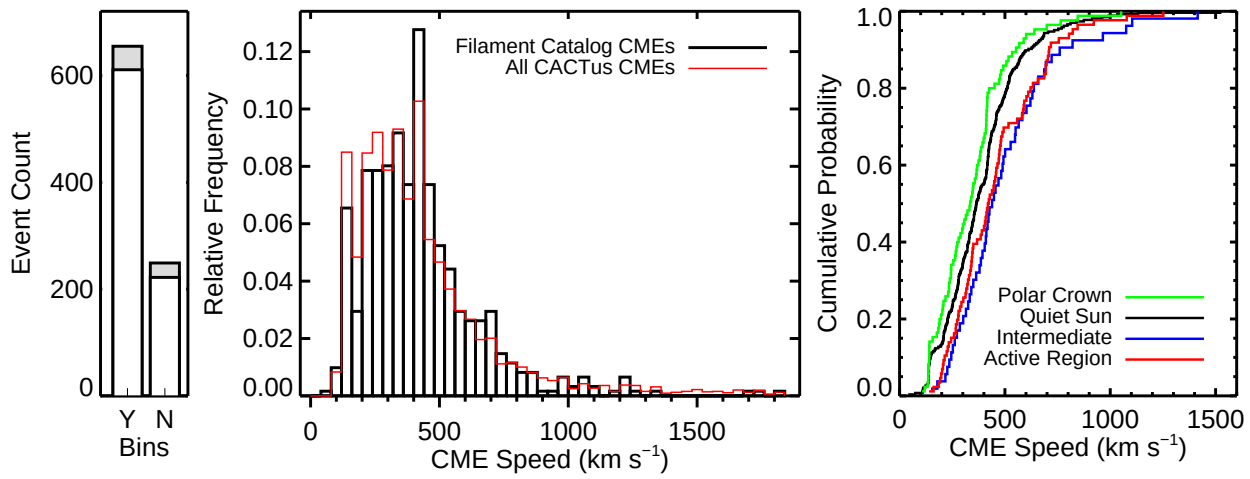


Figure 9. *Left*: Distribution of events with and without associated white-light CMEs. *Middle*: Overall CME speed distribution. *Right*: Cumulative CME speed distributions by type.

that a cavity was visible prior to eruption, and *during* (D) indicates that a cavity became visible during the eruption. Figure 8 provides two examples along with a bar plot of the results for all 363 limb events in the catalog. Including the ambiguous events (e.g. "Y?"), we find that 49% have no obvious cavity prior to eruption, 34% do, and 17% have cavities that become visible after the eruption onset.

By filament type, we find that cavities are apparent before and during the eruptions for 8% and 22% of AR, 23% and 25% of IP, 33% and 18% of QS, and 60% and 4% of PC eruptions, respectively. It is important to note that cavities are most apparent when the filament is large, oriented along the line-of-sight, and free of neighboring structures, so higher rates are expected for PC and QS prominences. Conversely, the compactness and proximity to active region arcades of AR and IP prominences explains why associated cavities are less frequently seen prior to eruptions and more frequently seen during eruptions, when motion makes the coherent structures more apparent. Finally, we note that additional processing such as radial filtering (Forland *et al.*, 2013) can improve cavity visibility, which may have resulted in additional detections if applied to our 193 Å observations.

3.8. Coronal Mass Ejections (CMEs)

Coronal Mass Ejections (CMEs) are large expulsions of plasma and magnetic fields that escape into the heliosphere. A strong association between CMEs and filament eruptions has been known for many years from high statistical associations (∼70%; Munro *et al.* 1979) and Hα emission in CME cores (Sheeley *et al.*, 1980). As described in the previous section, CMEs often exhibit a three-part structure that includes the overlying prominence cavity and embedded filament. A review of CME and prominence eruption associations is provided by Webb (2015). Complementary reviews on prominence eruption dynamics and space weather implications are also provided by Gopalswamy (2015) and Lugaz (2015), respectively. White-light coronagraphs have historically been the primary means by which CMEs are detected, and our associations are based on observations from the Large Angle Spectroscopic Coronagraph (LASCO; Brueckner *et al.* 1995) aboard the Solar and Heliospheric Observatory (SOHO; Domingo, Fleck, and Poland 1995). Our definition of "CME" is thus instrument-dependent, but it is important to note that the term refers to a physical process that is not limited to coronagraph observations.

Table 2. CACTus CME Speeds

Category[a]	Events	CME Speed (km s^{-1}) Min	Max	Mean ± SD[b]	Median ± MAD[b]
All CACTus	6368	91	1950	428 ± 277	367 ± 182
All Filament	609	41	1840	425 ± 228	390 ± 158
Active Region	85	140	1320	466 ± 219	425 ± 163
Intermediate	52	149	1710	515 ± 272	449 ± 182
Quiescent	266	41	1840	391 ± 204	365 ± 143
Polar Crown	85	107	1220	351 ± 184	337 ± 133
Full	264	112	1740	461 ± 225	422 ± 157
Partial	210	41	1230	390 ± 208	361 ± 151
Twist = Yes	306	108	1740	432 ± 233	380 ± 160
Twist = No	156	41	1840	380 ± 210	374 ± 147

[a]Subgroups exclude ambiguous events (e.g. Type = AR?).
[b]SD = Standard Deviation & MAD = Median Absolute Deviation.

We search for matching events using the Computer Aided CME Tracking catalog (CACTus[7]), which automatically detects CMEs, measuring both velocity and angular size. The speeds are averages of linear fits to radial height-time profiles that span the angular width of the CME and extend from 1.5 to 30 $R_\odot$ in height above the limb (Robbrecht and Berghmans, 2004). These measurements reflect all parts of the CME, but note that there is variation within the three-part CME structure, with leading edges tending to be 30 to 40% faster than core speeds (Gopalswamy *et al.*, 2003; Maričić, Vršnak, and Roša, 2009). In the few cases where LASCO or CACTus data are unavailable, we note the likelihood of a CME in the catalog with a question mark ("e.g. Y?"). We find that 72% of our eruptions have associated CMEs and 28% do not. Similar rates are found when the events are divided by type, with CME-associations found for 70% of AR, 75% of IP, 72% of QS, and 73% of PC eruptions.

Basic statistics are listed in Table 2 for several groupings, and Figure 9 shows the CME speed distributions, which exhibit lognormal profiles that have been reported in other works (Yurchyshyn *et al.*, 2005; Zhang and Dere, 2006; Bein *et al.*, 2011). We will see in §4 that this pattern emerges in the low corona. The average speed of CMEs associated with our filament eruptions is 430 km s^{-1}, which is essentially the same as for all CMEs detected by CACTus over the SDO mission lifetime. Moon *et al.* (2002) compare similarly-observed CMEs associated with flares versus filament eruptions. They found a similar average velocity for filament-eruption CMEs but also reported these to be ∼9% slower than the general population, which is not found here. This discrepancy may be due to the inclusion of false-positives in the CACTus catalog from transients related to previous CMEs or intensity variations in the slow solar wind that bias the total CACTus distribution toward lower speeds (Robbrecht, Berghmans, and Van der Linden, 2009).

We find, predictably, that full eruptions produce faster CMEs than partial eruptions by a factor of 1.2 on average. Full and partial eruptions have corresponding LASCO CMEs 95% and 81% of the time, respectively. Those that do not produce CMEs are generally

[7]CACTus CME catalog: http://sidc.oma.be/cactus/

very small, perhaps becoming confined or too diffuse to be detected at larger heights, or are oriented on the disk such that the opening angle is unfavorable for viewing by the coronagraph. Conversely, confined events lack CMEs 96% of the time. The remaining 4% either stimulate an eruption in a higher or neighboring structure, or the escaping filament material and/or magnetic structure was not perceptible in the AIA observations.

We also find that intermediate prominence eruptions are the most likely to be associated with CMEs and that their CMEs tend to be the fastest. On average, IP-CMEs are 1.1× faster than AR-, 1.3× faster than QS-, and 1.5× faster than PC-CMEs. The cumulative probability distributions shown in the right panel of Figure 9 indicate that the AR and IP curves are quite close. To test if their difference is statistically significant, we apply the k-sample Anderson-Darling (A_k^2) test, a non-parametric test that measures the deviation between an arbitrary number of empirical distribution functions (2 in this case) and provides a significance level for which the null hypothesis that the groups are drawn from the same distribution can be rejected (Scholz and Stephens, 1987). The A_k^2 statistic for the IP and AR distributions is -0.50, corresponding to a p-value of 0.59, well above the 0.05 level below which the distributions can be considered significantly different. We conclude, then, that our finding of enhanced CME speeds for IP versus AR eruptions is suggestive but not statistically significant. We do find a significant relationship between apparent twisting motions and CME speed, which will be discussed in §5.2.

4. Kinematics

Filament eruptions often exhibit distinct slow- and fast-rise phases, which has been explored in a number of case studies (e.g. Sterling and Moore 2004, 2005; Chifor *et al.* 2006; Sterling *et al.* 2007; Schrijver *et al.* 2008; Sterling, Moore, and Freeland 2011; Joshi and Srivastava 2011; Koleva *et al.* 2012). The slow portion is characterized by speeds of a few km s^{-1} or less that may persist for several hours or minutes for quiescent and active region filaments, respectively. Rapid acceleration to hundreds of km s^{-1} follows during the fast-rise phase, which may produce a CME or a confined eruption. The slow-rise phase is often attributed to gradual flux cancellation or emergence that builds and elevates the filament until it succumbs to an MHD instability or a fast-reconnection process that initiates the fast-rise phase (Sterling, Harra, and Moore, 2007; Sterling, Moore, and Freeland, 2011; Fan, 2015). We will consider the underlying mechanisms in greater detail with respect to our results in §5. While previous low-corona studies have primarily relied on close inspection of individual events or a small ensemble, we examine the kinematics of 106 eruptions in our catalog to determine general properties of the slow- and fast-rise phases. In particular, we consider the transition between the two stages, using an analytic approximation to determine the onset of the fast-rise phase.

4.1. Procedure

Eruptions on the limb were chosen for their heightened contrast and limited projection effects compared to those on the disk. Bulk motions are inferred by tracing the leading edges in 304 Å observations and fitting curves to the resultant height-time profiles. Figure 10 illustrates this process for a single event. To begin, we select the linear slice that best characterizes the overall trajectory of the filament (Panel A). Additional slices offset by two degrees in either direction are identically processed for error estimation. Emission along these lines is binned to 300 pixels and interpolated onto a uniform grid, yielding a spatial

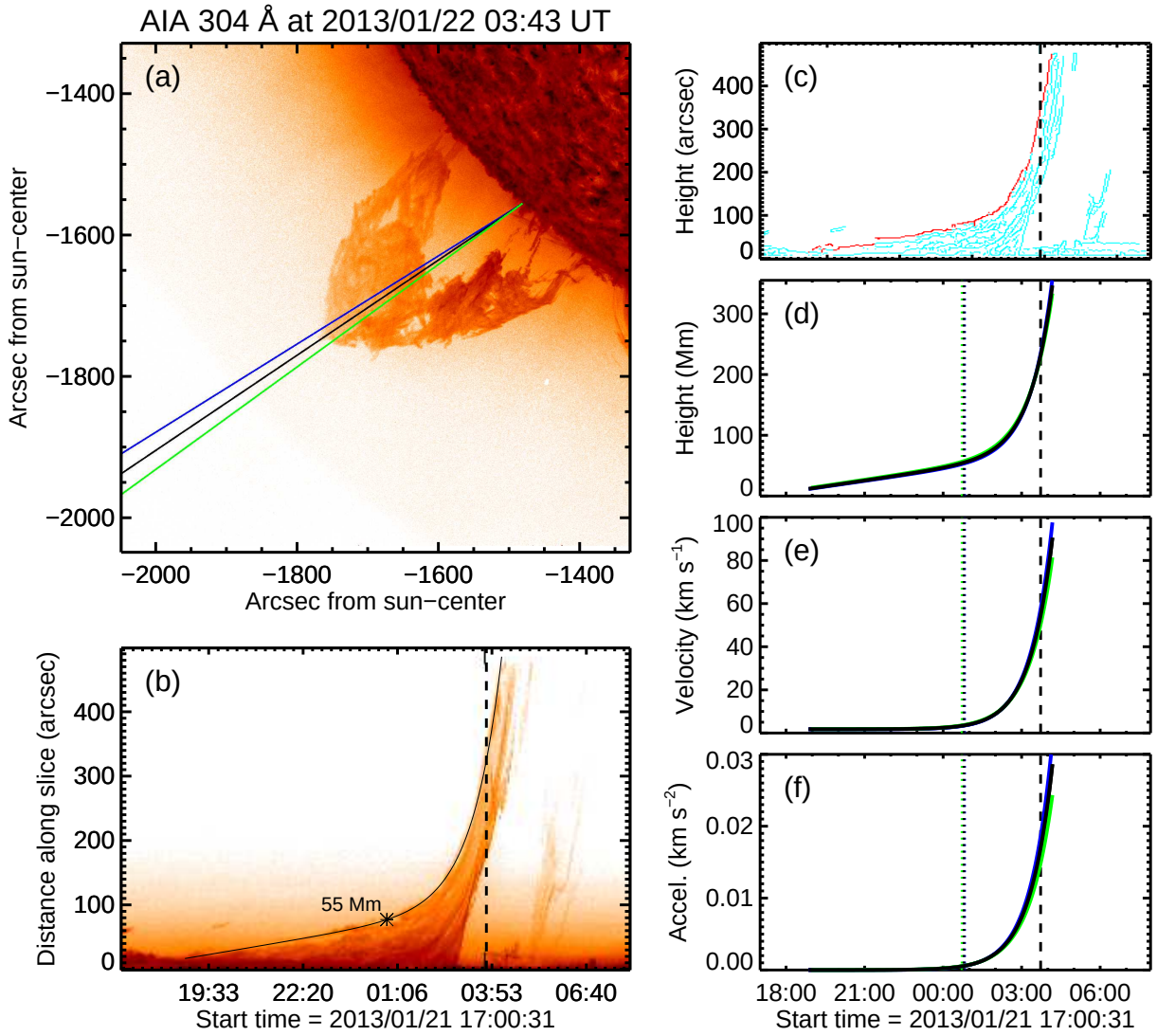


Figure 10. An illustration of the kinematics procedure using event No. 0620. (a) Trajectories used for tracking. The black slice is selected manually, and the others are offset by 2° in either direction. (b) Height-time image for the black slice in Panel A. The dashed line indicates the time shown in Panel A, the solid curve is the fit result, and the asterisk denotes the fast-rise onset point. (c) Output of the Canny edge detection algorithm applied to Panel B. The red pixels are used as individual height measurements. (d) Fit to the red pixels in Panel C. The dotted lines indicate the onset of the fast-rise phase, and the colors correspond to results from the different slices in Panel A. (e) Velocity and (f) acceleration profiles for the height profile in Panel D. A movie showing the evolution of the eruption along the main slice is provided on the catalog website.

resolution of ∼1.5”, which varies slightly depending on the length of the slice, dictated by FOV position. The resultant light curves are stacked against subsequent observations to produce height-time images like the one shown in Panel B. To further improve signal-to-noise, averages of 10 frames were used for each column measurement. This averaging corresponds to an effective exposure time of 29 seconds over a period of 2 minutes. Shorter averages were used for fast eruptions where a 2-minute time resolution was insufficient.

The height-time images are then further processed to improve contrast, which is typically limited to multiplying each row by its height to boost signal far from the limb and thresholding the image above some multiple of its median value. Smoothing is applied for

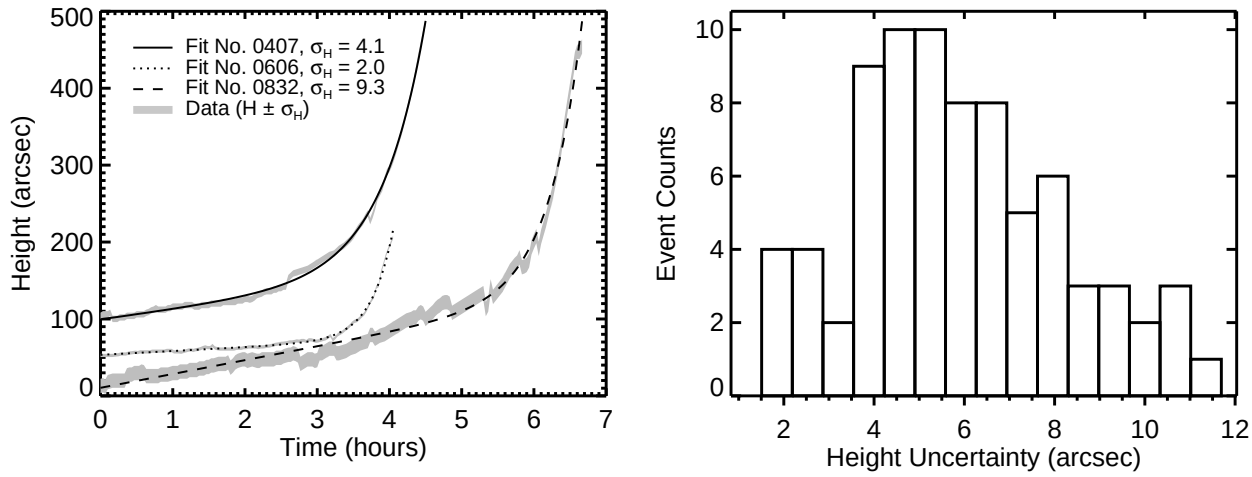


Figure 11. *Left*: Three examples with varying goodness-of-fits. *Right*: Histogram of height uncertainties, which correspond to the values required for $\chi^2_R = 1.0$ for the fits to Equation 1.

particularly noisy cases, and base differencing (background subtraction) is used for events where the contrast was especially low. The Canny edge detection algorithm (Canny, 1986) is then employed to extract leading edges from the height-time images. Panel C shows the application of the Canny algorithm to the image in Panel B. Pixels highlighted in red, which form the uppermost edge, are used as the individual height measurements. These points are extracted automatically once the edge detection has been applied, but their time range must be selected manually. This consideration is particularly important for the start time because it effectively defines the onset of the slow-rise phase.

4.2. Analytic Approximation

Several curves have been used in previous studies to fit the low-corona height evolution of eruptive prominences and CMEs in general. When there are distinct phases, the initial slow-rise profile is typically fit with a line, implying constant velocity (e.g. Sterling and Moore 2005), though at least one previous study has also employed a very slight constant-acceleration curve (Joshi and Srivastava, 2007). The fast-rise phase and rapid acceleration that initiates it has been approximated by exponential (e.g. Goff *et al.* 2005; Williams *et al.* 2005), exponential-plus-initial-velocity (Alexander, Metcalf, and Nitta, 2002), constant-acceleration (e.g. Gilbert *et al.* 2000; Kundu *et al.* 2004), and cubic (Schrijver *et al.*, 2008) curves. Cheng *et al.* (2013) present an equation that combines a linear curve to treat the slow-rise phase and an exponential to treat the fast-rise after a time offset:

$$h(t) = c_0 e^{(t-t_0)/\tau} + c_1(t - t_0) + c_2, \tag{1}$$

where $h(t)$ is height, t is time, and τ, t_0, c_0, c_1, and c_2 are free parameters. This model has the distinct advantage that both phases can be approximated by a single-function fit to the full dataset. It also provides a convenient method for determining the onset of the fast-rise phase, which can be defined as the point at which the exponential component of the velocity equals the linear (i.e. the total velocity is twice the initial), given by:

$$t_{\rm onset} = \tau \ln(c_1\tau/c_0) + t_0 \tag{2}$$

Table 3. Equation 1 $h(t)$ fit variable statistics for 78 events. t is in seconds relative to the start of observations, and h is in arcsec along the trajectories shown in Figure 13.

Variable	Min	Max	Mean ± SD	Median ± MAD
τ	260	19000	2700 ± 2500	2100 ± 1400
t_0	2600	130000	35000 ± 22000	33000 ± 16000
c_0	37	1400	240 ± 200	180 ± 130
c_1	0.00028	0.020	0.0029 ± 0.0027	0.0026 ± 0.0015
c_2	30	310	120 ± 61	110 ± 49

We find this approximation to be best suited for our study, which aims to characterize the the slow- and fast-rise phases of many events in a uniform way. Fitting is accomplished using MPFIT, a non-linear least squares curve fitting package for IDL (Markwardt, 2009). Panels D, E, and F of Figure 10 show the fit result and its time derivatives for our example event. Based on this approximation, we find that the initial slow-rise velocity is 1.8 ± 0.1 km s^{-1}, and the maximum velocity in the AIA FOV is 91 ± 7 km s^{-1}. The onset of the fast rise phase occurs at 00:48 UT ± 5 minutes at a distance of 55 ± 5 Mm along the fit trajectory, which begins with an initial height of 0.015 $R_\odot$ (∼10 Mm). The onset point is therefore 65 Mm above the limb *along the fit trajectory*, corresponding to a radial height of 64 ± 5 Mm. At the onset of the fast-rise phase, the acceleration is 0.57 ± 0.03 m s^{-2}, and the final acceleration is 29 ± 4 m s^{-2}. Table 3 lists the range of fit parameters found for the 78 events that can be satisfactorily described by this model. Details on the events that were not fit are given in §4.4.

Two strategies are employed to quantify uncertainty, and errors quoted are the sum of both. The first is to identically process two adjacent slices offset by 2° on either side of the original. On average, standard deviations from these results account for ∼65% of the velocity, acceleration, and time uncertainties, but they may contribute as little as 30% or as much as 90% for a particular event. The second strategy is to perform 100 Monte Carlo (MC) simulations to estimate uncertainties from the fit parameters by randomly varying our height measurements within some assumed error and refitting Equation 1. Since there are no standard errors for height measurements obtained by our edge detection method, the assumed height errors are chosen to yield a reduced chi-squared (χ^2_R) of 1.0 for the fit. This uncertainty is therefore a proxy for the goodness of fit. In the example above, height errors of 5.2″ are required for $\chi^2_R = 1.0$, which is very close to the average value of 5.8″ across all events. 5.8″ corresponds to ∼10 AIA pixels and around 4 pixels on the binned height-times images used to obtain the measurements. These values account for 58% of the fast-rise onset height errors on average, while uncertainties associated with the three separate slices and MC realizations typically account for 28% and 14% of the onset height uncertainties, respectively. The left panel of Figure 11 shows the data, errors, and associated fits for three examples with varying height uncertainties, and the right panel shows the total distribution of height uncertainties.

4.3. Solar Rotation

As we will see in the next section, slow-rise velocities of $\lesssim$ 1 km s^{-1} are found for a number of events and have also been reported in the literature (e.g. Sterling and Moore 2004; Isobe

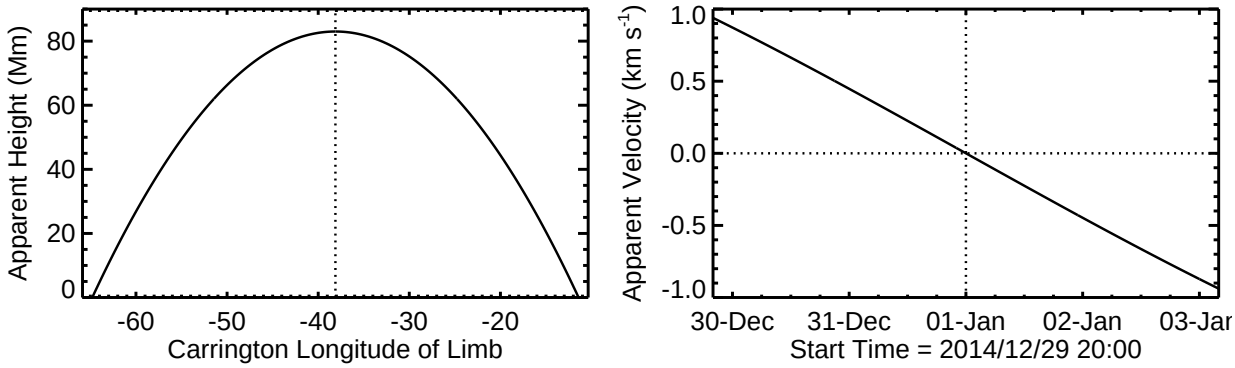


Figure 12. The effect of solar rotation on apparent height (left) and velocity (right) over a 4-day period for a prominence with an actual height of 83 Mm, a latitude of 45°, and a Carrington longitude of -38.1°.

et al. 2007; Liu *et al.* 2012b; Régnier, Walsh, and Alexander 2011; Reeves, McCauley, and Tian 2015). It is important to note that solar rotation alone can produce apparent rise and fall velocities of this magnitude. Accounting for this effect requires an understanding of the projection geometry and the longitudinal extent of the filament, consideration of which is beyond the scope of this work. The effect is minor and should be at least partially washed out in our statistics, but we nevertheless include this discussion to demonstrate that very small velocities for specific events should be treated with some caution.

Foullon and Verwichte (2006) provide the following expression for the height of an arbitrarily thin prominence sheet above the limb, as seen from Earth:

$$\frac{h(L)}{R_\odot} = \left(\frac{h_0}{R_\odot} + 1\right) \cos\left(L - L_0\right) - 1, \tag{3}$$

where $h(L)$ is apparent height, h_0 is actual height, L is the Carrington longitude of the limb, and L_0 is the Carrington longitude of the prominence. Figure 12 illustrates this effect over a 4-day period for a hypothetical prominence with a height of 83 Mm (our average fast-rise onset height) at a latitude of 45° and a Carrington longitude (L_0) of -38.1°, which corresponds to that of the east limb at 2014/01/01 00:00 UT. We see that rise and fall velocities approaching 1 km s^{-1} can be observed when a prominence begins to rotate onto and off of the limb. This could cause non-negligible over- or underestimations of the slow-rise velocites for the slower events in our sample, depending on their projection geometries and longitudinal extents.

4.4. Kinematics Results

Figure 13 summarizes the kinematics results, showing the positions and velocity profiles of each eruption. Of the 106 events, 78 (74%) have distinct slow- and fast-rise phases that are well-fit by the linear-plus-exponential model proposed by Cheng *et al.* (2013). These include 44 QS, 22 PC, 8 IP, and 4 AR eruptions. Representative examples of the remaining events that cannot be satisfactorily described by Equation 1 are shown in Figure 14. Corresponding to the figure panels, these events cannot be fit because they a) most commonly do not exhibit slow-rise phases or have no marked transition between phases, b) have rise profiles too complicated to fit into the simple two-phase dichotomy, c) have distinct phases but the transition into the fast-rise is decidedly not exponential, or d) exhibit dynamics that make it difficult to infer bulk motions from that of their leading edges. These events include 15 QS, 9 PC, 2 IP, and 2 AR events, and they are represented

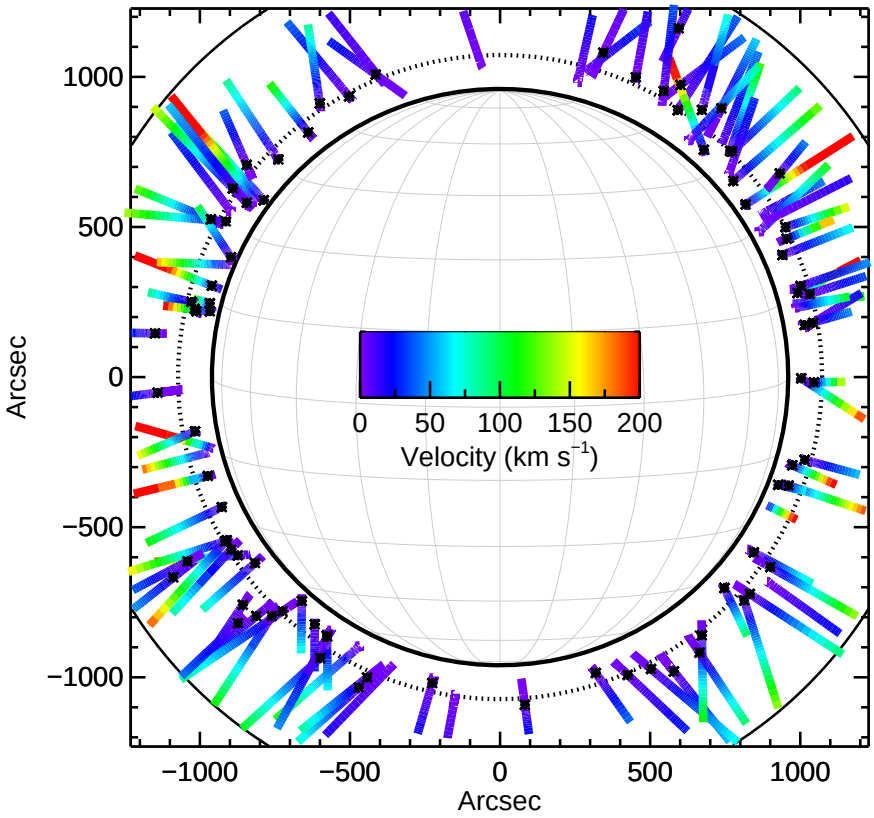


Figure 13. Positions and velocity profiles from the kinematics study. The asterisks denote the fast-rise phase onset point for events fit with Equation 1. Events without onset points are described by exponential functions. The dashed circle represents the average radial onset height of 83 Mm, and the rounded corner edges mark the boundary of the telescope's filter.

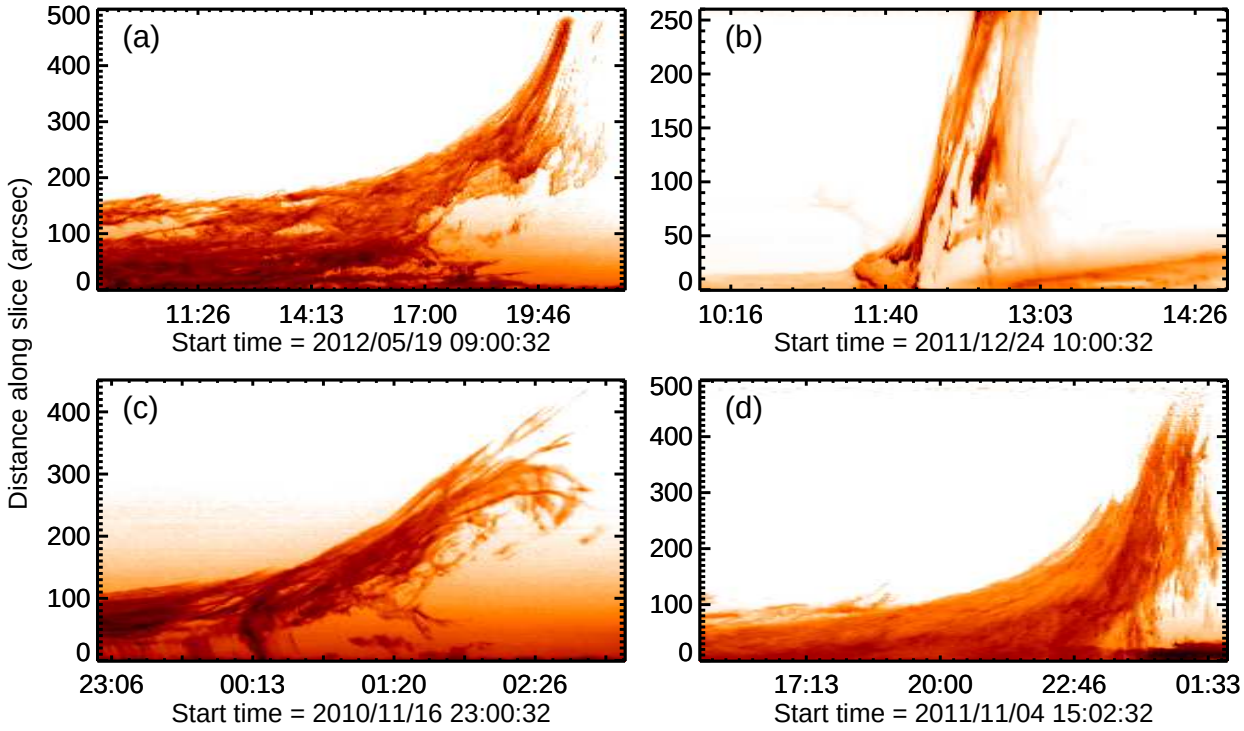


Figure 14. Representative examples of the "bad" events that could not be described by Equation 1 and were excluded from further analyses. See §4.4 text for details.

Table 4. Kinematics Results.

Parameter	Min	Max	Mean ± SD	Median ± MAD	$(\mu \pm \sigma)^a$	$(A^2)^b$
$h_{\rm onset}{}^c$ (Mm)	27	237	83 ± 41	71 ± 32	4.3 ± 0.51	0.35
$\Delta h_{\rm onset}{}^d$ (Mm)	2.6	89	29 ± 22	22 ± 17	3.1 ± 0.86	0.37
$\Delta t_{\rm slow-rise}$ (hrs)	0.36	23	4.4 ± 3.7	3.2 ± 2.7	1.1 ± 0.93	0.37
$v_{\rm slow-rise}$ (km s^{-1})	0.21	16	2.1 ± 2.1	1.9 ± 1.1	0.50 ± 0.67	0.81
$v_{\rm fov-max}$ (km s^{-1})	6.0	417	106 ± 85	82 ± 60	4.4 ± 0.83	0.18
$v_{500''}{}^e$ (km s^{-1})	13	753	183 ± 169	126 ± 110	4.8 ± 0.84	0.38
$a_{\rm onset}$ (m s^{-2})	0.032	29	1.9 ± 3.7	0.82 ± 1.5	-0.28 ± 1.1	0.53
$a_{\rm fov-max}$ (m s^{-2})	0.29	970	111 ± 183	40 ± 96	3.6 ± 1.5	0.38
$a_{500''}{}^e$ (m s^{-2})	0.64	1760	199 ± 362	57 ± 175	4.0 ± 1.6	0.43
$n_{\rm onset}{}^f$	0.69	2.0	1.1 ± 0.28	1.1 ± 0.22	0.089 ± 0.25	0.56

[a] Lognormal fit parameters.
[b] Anderson-Darling goodness-of-fit statistic; low values imply better fits.
[c] Radial fast-rise onset height.
[d] Slow-rise phase displacement along fit trajectory (relative onset height).
[e] Parameters at 500″ above the limb; excludes 6 confined events.
[f] Decay index at the fast-rise onset point; see Section 5.1.

in Figure 13 with exponential fits. While it would be interesting to consider these misfits in detail, they are excluded from all further analysis and left for future work.

It is also clear that the kinematics study is biased toward QS and PC eruptions from the proportion of AR and IP events in this sample compared to the catalog. This selection effect is primarily due to the semi-automated method described in §4.1, which requires that the trajectory be free of additional structures that cannot be easily subtracted away. The more dynamic environments of AR and IP filaments thus precluded a clean isolation of the eruption front by our edge detection method in a number of additional events that we attempted to process. This effect is exacerbated by the smaller size and lower initial heights of AR filaments because they consequently spend less time above the limb. Several otherwise suitable events were also excluded because a significant portion of their slow-rise phases occurred behind the limb or on the disk. For this reason, our AR sample includes somewhat larger filaments than average for that type. This bias combined with the small number of events means that our AR results may not accurately represent the general population, and additional work is therefore needed to obtain robust statistics. Refinements to our technique can likely improve its applicability, but that is beyond the scope of this work.

Figures 15, 16, and 17 show distributions of the fast-rise onset heights, slow-rise durations, velocities, and accelerations for the 78 events fit with Equation 1. Cumulative distributions are also plotted for QS and PC events, along with a single curve for AR and IP eruptions, which are combined due to their small sample sizes. The histograms are best described by lognormal distributions, reminiscent of CME speeds (Yurchyshyn *et al.*, 2005; Zhang and Dere, 2006; Bein *et al.*, 2011), and lognormal fits are plotted in red. An independent variable, x, is said to be lognormally-distributed when $\ln(x)$ has a normal distribution. Note that Figure 17 plots the natural logarithm of acceleration because of the particularly large ranges and therefore exhibits a normal distribution. Physically, lognormal distributions may arise when a quantity is the multiplicative product of several independent

Table 5. Mean ± SD Kinematics Results by Type.

Parameter	Type				
	All	AR	IP	QS	PC
Event Count	78	4	8	44	22
$h_{\rm onset}$ (Mm)	83 ± 41	48 ± 16	60 ± 24	82 ± 42	101 ± 38
$\Delta h_{\rm onset}$ (Mm)	29 ± 22	13 ± 11	20 ± 9.4	25 ± 19	43 ± 24
$\Delta t_{\rm slow-rise}$ (hrs)	4.4 ± 3.7	1.2 ± 0.82	2.2 ± 1.9	3.7 ± 2.8	7.2 ± 4.4
$v_{\rm slow-rise}$ (km s^{-1})	2.1 ± 2.1	2.3 ± 0.41	4.1 ± 4.8	1.9 ± 1.5	1.7 ± 0.89
$v_{\rm fov-max}$ (km s^{-1})	106 ± 85	158 ± 95	218 ± 111	108 ± 74	53 ± 33
$v_{500''}$ (km s^{-1})	183 ± 169	359 ± 180	390 ± 216	183 ± 146	80 ± 52
$a_{\rm onset}$ (m s^{-2})	1.9 ± 3.7	4.1 ± 3.4	6.6 ± 9.2	1.4 ± 1.6	0.60 ± 0.49
$a_{\rm fov-max}$ (m s^{-2})	111 ± 183	320 ± 261	336 ± 316	97 ± 132	21 ± 24
$a_{500''}$ (m s^{-2})	199 ± 362	505 ± 402	628 ± 589	176 ± 305	33 ± 47
$n_{\rm onset}$	1.1 ± 0.28	1.0 ± 0.18	1.1 ± 0.21	1.2 ± 0.29	1.1 ± 0.28

variables, suggesting a multiplication of several independent processes, as opposed to the sum of independent variables for a normal distribution.

The lognormal probability, $f(x)$, and cumulative probability, $F(x)$, distributions are given by:

$$f(x) = \frac{1}{\sqrt{2\pi}\sigma x}\exp\left(-\frac{(\ln x - \mu)^2}{2\sigma^2}\right); \quad F(x) = \frac{1}{2} + \frac{1}{2}\mathrm{erf}\left(\frac{\ln x - \mu}{\sqrt{2}\sigma}\right), \tag{4}$$

where μ is the mean and σ is the standard deviation of $\ln(x)$. A least squares fit to the empirical cumulative probability distribution is used to approximate $F(x)$, avoiding the unnecessary binning that would be needed to fit $f(x)$. We employ the modified Anderson-Darling (A^2) test to quantify the goodness-of-fit, which tells us if the empirical distribution is *unlikely* to be drawn from the fitted distribution. The null hypothesis for this test is that the empirical distribution *is* drawn from the fitted distribution, which can be rejected at the 0.05 significance level if $A^2 > 0.752$ and at the 0.25 level if $A^2 > 0.470$ (D'Agostino and Stephens, 1986). Low values of A^2 therefore imply better fits. Table 4 lists several statistical measures for each of the total distributions, including the lognormal fit parameters and A^2 values, and Table 5 lists the arithmetic means and standard deviations for each quantity by filament type. With reference to Bein *et al.* (2011) and Limpert, Stahel, and Abbt (2001), we use $\mu^* = e^{\mu}$ and $\sigma^* = e^{\sigma}$ to refer to the median and multiplicative standard deviation of the fitted distribution, respectively. The 68% confidence interval for a lognormal distribution then spans from $\mu^* \div \sigma^*$ to $\mu^* \times \sigma^*$.

4.4.1. Fast-Rise Phase Onset Heights & Slow-Rise Durations

The left panel of Figure 15 shows the distribution of radial fast-rise onset heights ($h_{\rm onset}$) derived from the prominence positions at $t_{\rm onset}$ (Equation 2). We find mean and median values of 83 and 71 Mm, respectively, and the fitted lognormal distribution has a median (μ^*) of 74 Mm and a 68% confidence interval that spans from 44 to 122 Mm. Compared to

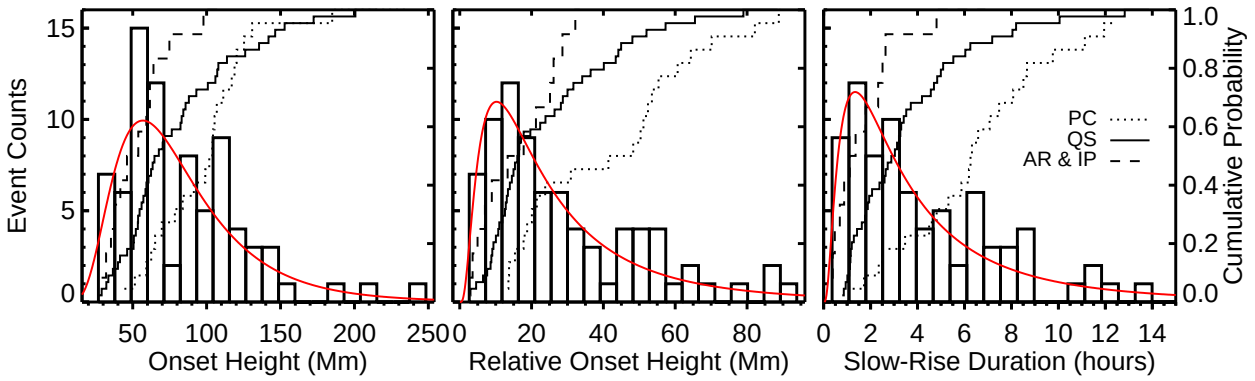


Figure 15. *Left*: Radial fast-rise onset heights. *Center*: Slow-rise phase displacements along the fit trajectories. *Right*: Slow-rise phase durations. The histograms show the overall count distributions (left axes), the black curves show the cumulative probability distributions for specific types (right axes), and the red curves show lognormal fits to the histograms.

QS eruptions, for which $\overline{h}_{\rm onset} = 82$ Mm, AR and IP filaments tend to reach their critical points at 0.59× and 0.74× lower heights, respectively, while PC events transition into the fast-rise phase at 1.24× larger altitudes. We can also consider the distances traveled along the fit trajectories, which may be non-radial (see Figure 13), by subtracting the initial leading edge positions from their positions at $t_{\rm onset}$. This relative onset height ($\Delta h_{\rm onset}$) reflects the magnitude of the slow-rise phase displacement, and its distribution is shown in the middle panel of Figure 15. $\mu^* = 21.3$ Mm for $\Delta h_{\rm onset}$, very close to the actual median value of 21.8 Mm, and the 68% confidence interval ranges from 9 to 50 Mm. The relative onset heights are 0.51× lower, 0.80× lower, and 1.75× higher for AR, IP, and PC events, respectively, compared to the QS average of 25 Mm. Some of the differences between both the radial and relative onset heights across filament types can be attributed to a positive correlation between latitude and onset height found for the entire sample, which will be discussed in §5.1 with respect to the decay index of the magnetic field.

Liu *et al.* (2012a) also examine the fast-rise onset height, which they refer to as the critical height, using STEREO observations of 362 prominences that were detected and tracked by an automated system (Wang *et al.*, 2010). Height-time measurements from the fast-rise phase were fit with a line, and the critical height was defined as the intersection between this line and the height profile prior to the fast-rise phase. This method would give somewhat larger heights if applied here, since our onset heights refer to the base of an exponential growth curve (Equation 2), but this difference is very small compared to the range of heights found. Liu *et al.* (2012a) find an average critical height of 77 Mm (0.11 $R_\odot$), which is 6 Mm less than our average but still well within one standard deviation.

The right panel of Figure 15 shows the distribution of slow-rise phase durations, or the time required to cover $\Delta h_{\rm onset}$. The average across all types is 4.4 hours, and the type averages are sorted as expected, with AR and PC events at the low and high ends. The 68% confidence interval spans 1.2 to 8.0 hours, which covers most of the values reported in the literature (e.g. Sterling and Moore 2005; Joshi and Srivastava 2007; Reeves, McCauley, and Tian 2015). The minimum slow-rise phases were 22 and 24-minutes for an IP and AR event, respectively. The short end found in the literature is around 10 minutes, reported by Sterling and Moore (2005) for an AR eruption, though the authors note that the filament appeared to begin rising at least 10 additional minutes earlier. Chifor *et al.* (2006) report and AR filament slow-rise duration of 34 minutes for a separate event. Our sample of AR events is quite small for reasons described above, which likely contributes to the paucity of

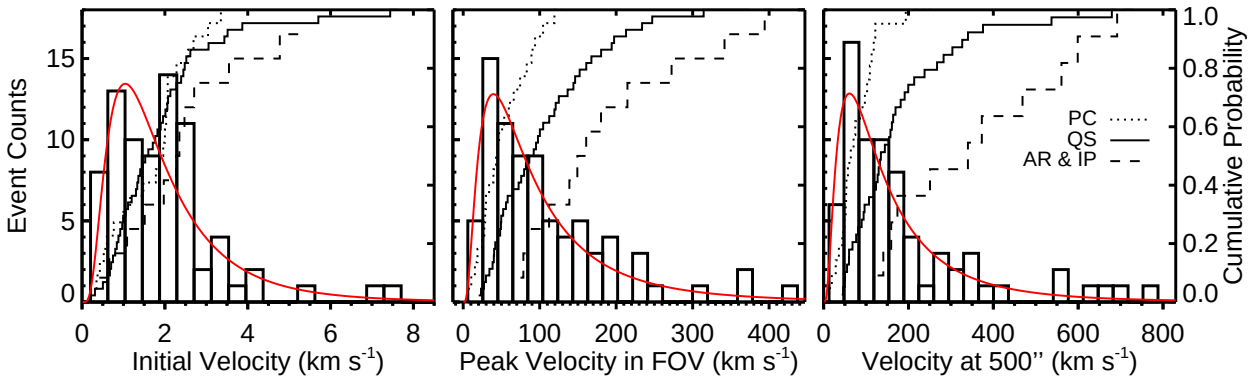


Figure 16. *Left*: Slow-rise velocity. *Center*: Peak velocity in FOV. *Right*: Velocity at 500" above the limb (projected). The histograms, curves, and axes are as in Fig 15.

brief slow-rise phases and biases our lognormal fit toward longer durations. AR eruptions may also exhibit only exponential growth (i.e. have no slow-rise phase), such as the two AR events that could not be fit by Equation 1 in our initial sample and the event described by Williams *et al.* (2005). In these cases, the slow-rise phase may be non-existent or may simply be indiscernible by the analysis technique or instrument resolution. At the other end of the spectrum, the longest slow-rise phase is 23 hours for a PC eruption. This event is an extreme outlier at 3 hours outside of the 95% confidence interval upper bound ($\mu^* \times \sigma^{*2}$) for the lognormal fit, already expected to be biased toward long durations, and indeed we could find no counterparts in the literature. Liu *et al.* (2012b) report a slow-rise phase duration of ∼10 hours, which is one of the largest values previously reported and is much closer to the longer slow-rise phases we observe, excluding the outlier.

4.4.2. Velocity & Acceleration Distributions

Moving to the velocity distributions plotted in Figure 16, we find that the initial slow-rise speeds range from a minimum of 0.2 to a maximum of 16 km s^{-1}. Recalling §4.2, these values are derived from the linear component of Equation 1 and dominate the total velocity until the exponential component of the curve contributes equally at $t_{\rm onset}$ (Equation 2). The lognormal fit to the $v_{\rm slow-rise}$ distribution is particularly bad, with $A^2 > 0.752$, meaning that we can reject the hypothesis that the velocities are lognormally-distributed with a p-value < 0.05. Instead, the histogram is double-peaked with enhanced slow-rise velocities around 1 and 2 km s^{-1}. However, if we consider only QS events, the values follow a lognormal distribution very closely to $A^2 = 0.25$. (In fact, all of the QS-only distributions except for $v_{\rm fov-max}$ are somewhat better-fit by lognormal profiles than the corresponding total distributions, with $\overline{A^2} = 0.31$ vs. 0.42. While we do not show the type-specific histograms and fit profiles, the characters of their distributions may be gleaned from the cumulative distributions in Figures 15–17.)

The total $v_{\rm slow-rise}$ distribution deviates from log-normality primarily because the PC-only distribution, which has a large enough sample to draw meaningful conclusions from, is *not* lognormal to a significance of over 99% ($A^2 = 1.1$). Instead, it is better fit by a single Gaussian with a mean of 1.7 and a variance of 1 km s^{-1} ($A^2 = 0.55$). The low number of events in the AR and IP distributions preclude us from concluding anything about their general $v_{\rm slow-rise}$ distributions, but the limited information hints at log-normality for IP and normality for AR eruptions. In light of this, the other panels of Figure 16 reveal an intriguing development. The middle panel shows the maximum velocities attained in the AIA FOV, and the right panel shows the fit velocity at a fixed height of 500″ above the

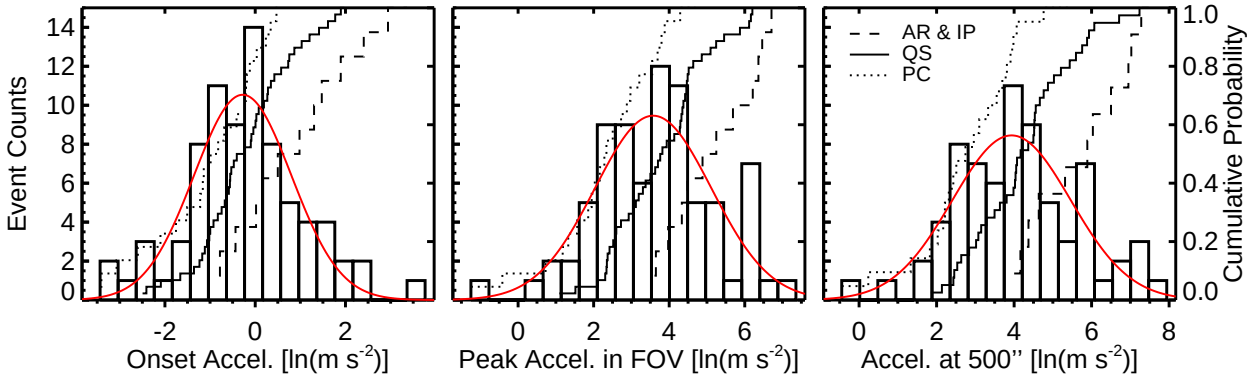


Figure 17. *Left*: Fast-rise onset acceleration. *Center*: Peak acceleration in FOV. *Right*: Acceleration at 500" above the limb (projected). The histograms, curves, and axes are as in Fig 15.

limb, which is roughly the maximum height that AIA can observe for structures near the FOV corners. These latter velocities are included because the maximum observable height, where $v_{\mathrm{fov-max}}$ is generally taken, varies depending on FOV position (see Figure 13). Low-latitude fits are therefore projected for the 500″ comparison, and 6 confined events are excluded because the filament material does not reach that height.

Both of these velocity distributions exhibit robust lognormal profiles despite having emerged from a slow-rise distribution that is significantly less so. This is true even for the PC-only distributions ($A^2 \approx 0.33$). Lognormal profiles are also found for each of the acceleration distributions shown in Figure 17, which is particularly significant for the fast-rise onset accelerations (a_{onset}) because it indicates that the velocity distribution shift begins immediately at the start of fast-rise phase. We might draw two inferences from this. First, the normal distributions of PC and perhaps AR slow-rise velocities hint at a more uniform process than the IP and QS counterparts. This finding may be understood in terms of the more varied environments and size-scales of IP and QS filaments, which provide a more diverse set of influences to impact the slow-rise pace. Second, the lognormal distributions for the fast-rise velocities of all types hint at the multiplicative contribution of several processes. This result may be understood in terms of the various, and not necessarily mutually exclusive, fast-rise onset mechanisms (to be discussed further in §5) in combination with environmental influences. We also see that the lognormal distribution of CME speeds reported in previous works emerges early in the height evolution of prominence eruptions.

Now we turn briefly to how our velocity and acceleration values differ by filament type. As with the CME speeds in §3.8, we find that IP eruptions are generally the fastest of the four types. The average IP slow-rise velocity is 4.1 km s^{-1}, which is about 1.8×, 2.2×, and 2.4× faster than the AR, QS, and PC averages, respectively. Similar relationships between types are found for the other velocity and acceleration quantities. Accelerations at t_{onset} range from a minimum of 0.03 m s^{-2} for a PC eruption to a maximum of 29 m s^{-2} for an IP event, with an overall average value of 1.9 and a 68% confidence interval of 0.25 to 2.3 m s^{-2}. After the fast-rise onset, the velocities grow exponentially to reach values at 500″ above the limb of between 13 km s^{-1} for the slowest PC eruption and 750 km s^{-1} for the fastest IP event. The median value upon exiting the AIA FOV is 82 km s^{-1}. See Table 4 and Table 5 for the full list of statistical parameters. These values are broadly consistent with those reported in the literature, much of which has already been referenced.

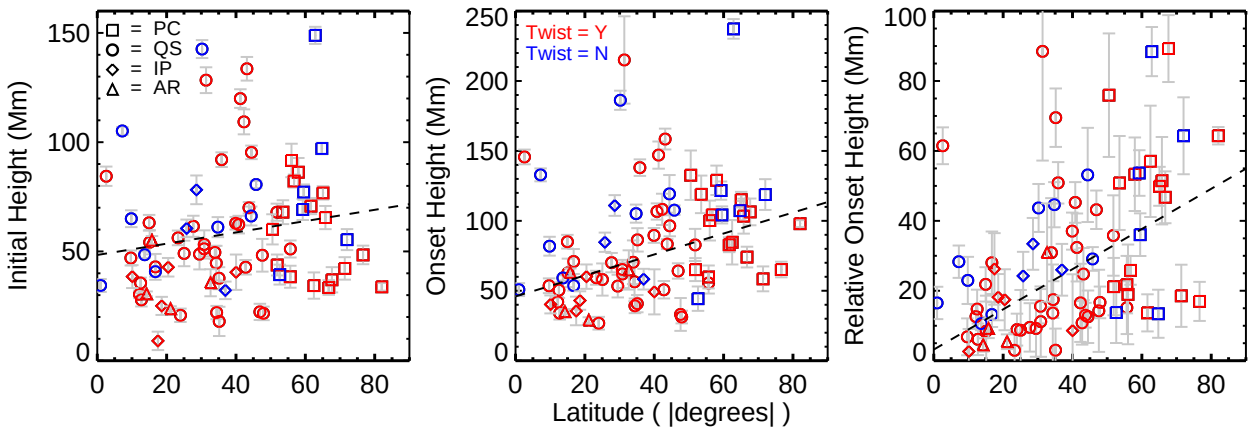


Figure 18. Latitude versus initial height (left), onset height ($h_{\rm onset}$, middle), and relative onset height ($\Delta h_{\rm onset}$, right), where the latitudes are those of the onset points in Figure 13.

4.5. Online Catalog Kinematics Content

The online catalog includes a version of Figure 10 and the associated movie for each of the 106 events in the kinematics study. Text files files containing the height vs. time data, fit parameters, and essential results are also provided. Information on finding and using these files is provided on the catalog website.

5. Discussion

A few interesting patterns emerge from our results that are relevant to the broader discussion on filament eruption triggering. Initiation mechanisms for the fast-rise, rapid acceleration phase (or for the entire eruption if there is no slow-rise) are generally divided between ideal MHD instabilities and fast magnetic reconnection processes (see review by Fan 2015). The former includes the helical kink instability, discussed in §3.5, and the torus instability, which occurs when a toroidal flux rope rises to a critical height above which it cannot be contained by the overlying magnetic field (Kliem and Török, 2006). Considering reconnection triggers, flux emergence (Chen and Shibata, 2000) or cancellation (van Ballegooijen and Martens, 1989) may lead to reconnection that stimulates the eruption, or breakout reconnection in the overlying field may prompt an eruption (Antiochos, DeVore, and Klimchuk, 1999). These mechanisms are not necessarily mutually exclusive, and reconnection may also facilitate an eruption triggered by the catastrophic loss of MHD equilibrum (Lin and Forbes, 2000). Several mechanisms have also been proposed for the slow-rise phase, perhaps the most common of which is flux cancellation that increases the twist of a filament, slowly buoying it until an MHD instability or reconnection process triggers rapid acceleration (e.g. Amari *et al.* 2010; Aulanier *et al.* 2010). Alternatively, Reeves *et al.* (2010) simulate the initial slow rise of a flux rope CME by means of resistive diffusion, and Fan and Gibson (2007) discuss the possibility of a flux rope emerging from beneath the photosphere.

5.1. Onset Height, Latitude, & Decay Index

Figure 18 plots the initial prominence height, onset height, and relative onset height versus latitude, where the latitudes are those of the onset points in Figure 13. Recalling §4.4.1, the onset height ($h_{\rm onset}$) is a radial height above the limb, while the relative onset height

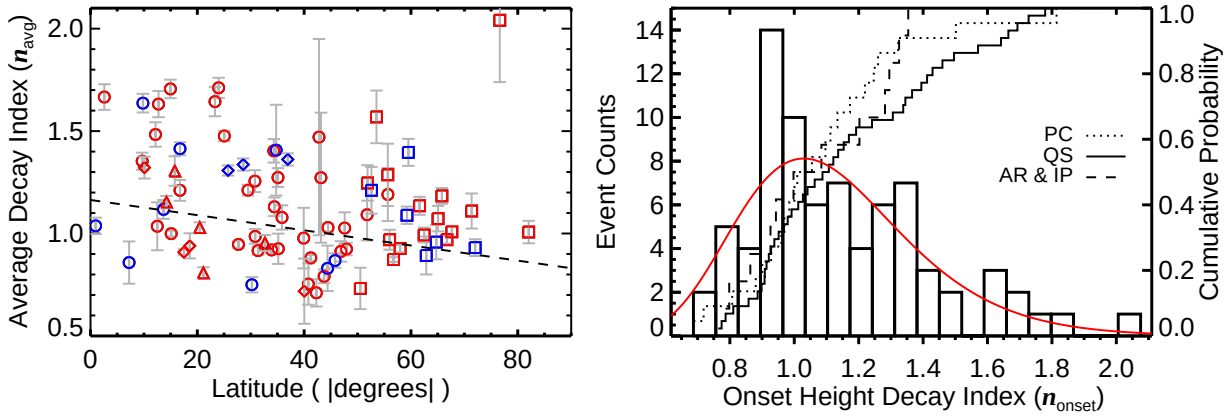


Figure 19. *Left:* Average decay index between 42 and 105 Mm vs. latitude. Symbols and colors are as in Fig. 18. *Right:* Distributions of the decay indexes at the fast-rise onset height. The histogram, curves, and axes are as in Fig. 15–17.

($\Delta h_{\rm onset}$) refers to a displacement along a particular fit trajectory. We find a positive correlation between latitude and onset height, with a Pearson's correlation coefficient (r) of 0.30 and a p-value of 0.008. The relationship strengthens if we instead consider the relative onset height ($r = 0.43$, $p = 7{\times}10^{-5}$) or slow-rise phase duration ($r = 0.50$, $p = 3{\times}10^{-6}$). This effect is distinctly global in that if we divide the data into latitude bins of 20°, for instance, the correlation within a given bin is insignificant or non-existent. It is also distinct from a relationship between latitude and the initial prominence height, for which there is a weak and statistically insignificant positive correlation ($r = 0.14$, $p = 0.13$) that disappears if IP and AR events are excluded.

The maximum height of non-eruptive prominences was suggested as a parameter of the magnetic field by Leroy, Bommier, and Sahal-Brechot (1984). Makarov *et al.* (1992) expanded on this, using height variations among prominences of the same latitude as a proxy for longitudinal variations in the background field strength. Makarov (1994) also reported that the height of polar crown prominences (latitudes greater than 55°) decreased with increasing latitude using observations of many prominences over several solar cycles. We see this effect to some extent in our initial height data for the PC-only sample, which exhibit a minor negative correlation (r = -0.21, p = 0.35) between latitude and initial height. Upon erupting, the PC-only data shift to no correlation with latitude for onset height and a minor positive correlation ($r = 0.17$, $p = 0.45$) for relative onset height.

The critical height of a flux rope, above which no stable equilibria exist, can be related to a critical threshold in the vertical gradient of the magnetic field, or decay index (Filippov and Den, 2000):

$$n = -\frac{d(\ln \mathbf{B})}{d(\ln h)}, \tag{5}$$

where $\mathbf{B}$ is the strapping field and h is height above the photosphere. This is the essential concept of the previously-mentioned torus instability, which refers specifically to toroidal (curved) flux ropes but may sometimes be used more generally to encompass all geometries. The critical decay index ($n_{\rm cr}$) for loss of confinement depends principally on the assumed flux rope configuration and is canonically 1.0 for the straight (van Tend and Kuperus, 1978) and 1.5 for the toroidal (Bateman, 1978) thin current channel approximations. Both geometries represent limiting cases of the same physical process (Démoulin and Aulanier,

2010). Recent theoretical calculations and numerical simulations have found n_{cr} values between 1.0 and 2.0 under various assumptions that better approximate coronal conditions (Kliem and Török, 2006; Fan and Gibson, 2007; Aulanier *et al.*, 2010; Démoulin and Aulanier, 2010). If we assume that many of the events in our sample are driven to erupt by this sort of mechanism, then a positive correlation between latitude and fast-rise onset height implies that the decay index is smaller at high latitudes for a given altitude.

To test this hypothesis, we estimate the decay index along our eruption trajectories using potential field source surface (PFSS) extrapolations of the coronal magnetic field based on line-of-sight magnetograms from the SDO's Helioseismic and Magnetic Imager (HMI, Scherrer *et al.* 2012). Decay index maps are obtained for the plane of the sky through Sun-center using the SolarSoft IDL software package FORWARD[8] (Gibson *et al.*, 2014), which is capable of forward modeling various observables but in this case simply provides a convenient interface for SolarSoft's PFSS package[9]. Details on the PFSS model are given by Schrijver and De Rosa (2003). For each event, we record the decay index at the fast-rise onset height (n_{onset}) and the average decay index between 42 and 105 Mm above the limb (n_{avg}), the range of which is chosen for consistency with Liu (2008). The left panel of Figure 19 shows n_{avg} versus latitude, and we do find the expected negative correlation (r = -0.22, p = 0.06). This result, combined with the slight positive correlation between initial height and latitude, nicely explains the positive correlations between latitude and the related measures of fast-rise onset height, relative onset height, and slow-rise duration.

The right panel of Figure 19 shows a histogram of the fast-rise onset height decay indexes, and basic statistics are listed in Tables 4 and 5. It is interesting to note that the n_{onset} distribution clusters around 1.0, closer to the straight flux rope approximation than the curved. The average value is 1.1 and is essentially the same for all four filament types, despite their differences in kinematics parameters, particularly onset height. This result is generally consistent with Filippov and Den (2001) and Filippov (2013), who also find critical decay indexes of around 1.0 for observed quiescent filament eruptions and therefore suggest that the forces associated with the axis of curvature are essentially unimportant for the equilibria of coronal flux ropes. However, we also find that a significant fraction (27%) of our events have critical decay indexes greater than 1.3. Indeed, our results span the full range of aforementioned theoretical n_{cr} values derived from various flux rope and simulation configurations. We also find that 38% of our events begin their fast-rise phases with decay indexes of less than 1.0 and 15% do so with $n_{onset} < 0.9$. This finding suggests that an appreciable fraction of the eruptions are initiated by other means, such as reconnection or the kink instability.

Some limitations to our decay index estimates should be noted. First, we are looking at regions on the limb, where the PFSS extrapolations are constrained by observations a few days before or after the eruptions for the west and east limbs, respectively. Such time offsets are especially limiting for active regions, which are very likely to have evolved over those periods. Second, we use single values in the plane of the sky, which may not be perfectly aligned with a given filament. These considerations are particularly important for the discussion of eruption mechanisms because relatively small changes in the decay index can imply significant differences in the initiation process. They might also explain two peculiarities in our decay index results. The curvature of AR region filaments, with their shorter lengths, is generally thought to be more important compared to that of their more

[8]SolarSoft IDL FORWARD Package: http://www.hao.ucar.edu/FORWARD/

[9]SolarSoft IDL PFSS Package: http://www.lmsal.com/~derosa/pfsspack/

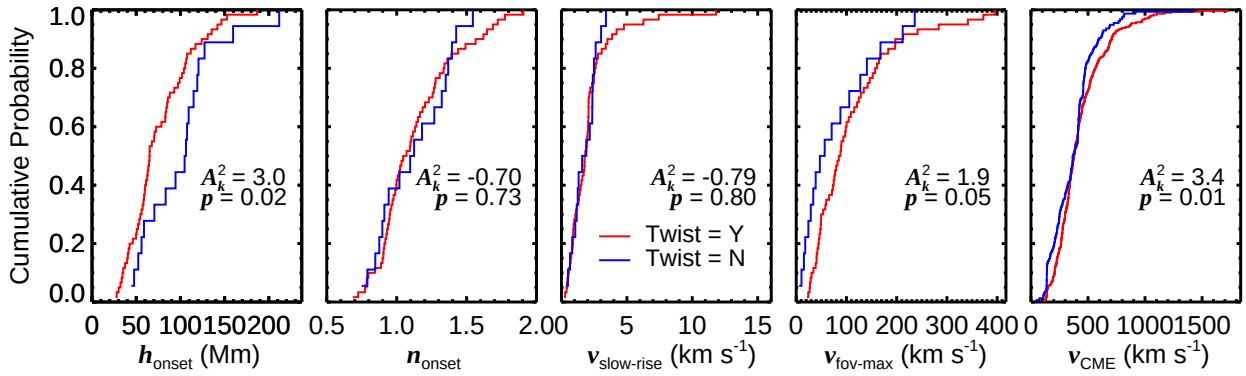


Figure 20. Empirical cumulative probability distributions for events with and without apparent twisting motions (see §3.4). The right panel (CME speed) covers the entire catalog, while the others include the 78 events in the kinematics study fit with Equation 1.

extended QS counterparts, meaning that AR n_{cr} thresholds should be closer to the toroidal approximation of ∼1.5. We instead find an average n_{onset} of 1.0 for the 4 AR events in our sample, which might be due to the PFSS limitations. There is also a conspicuous outlier in Figure 19, with a high latitude and large decay index. This filament (No. 0934) appears to be inclined such that the plane-of-sky decay index is not appropriate. More careful modeling and the use of STEREO observations to triangulate the filament positions would improve the decay index estimates. We will discuss possibilities for additional work on this topic in §5.3.

5.2. Kinematics & Twist

It is also interesting to consider possible relationships between kinematics and apparent twisting motions. Referring to §3.4, "apparent twist" may include motion that is induced during the eruption by surrounding features (i.e. the "roll effect") or, more commonly, motion that is likely to be indicative of the intrinsic flux rope twist, such as untwisting motions observed in filament footpoints near the end of an event. We hypothesize that on average, eruptions exhibiting twisting motions will have had greater helicity at their fast-rise onset points compared to those with no apparent twisting motions. Given this expectation, it is interesting to note that all but 2 of the 18 events with no apparent twist lie very close to or above the fit lines in the middle and right of Figure 18 (latitude vs. onset-height). On average, events with no twist begin their fast-rise phases at 1.4× larger heights, and comparing the cumulative distributions in the left panel of Figure 20 indicates a statistically significant difference ($A_k^2 = 3.0$ and $p = 0.02$). This result may be attributed to differences in the eruption mechanisms that preferentially affect more or less twisted filaments. One possibility is that highly-twisted flux ropes are more susceptible to the kink instability compared to less-twisted structures, which are more likely to succumb to the torus instability. These mechanisms should produce populations of lower and higher fast-rise onset heights, respectively, which would be superposed on a scatter of reconnection-driven events. The right panel of Figure 18, in particular, exhibits a pattern somewhat similar to this.

Fan and Gibson (2007) find from MHD simulations that the field decreases with height more slowly for the kink instability compared to the torus instability. We might therefore expect to see differences in the distributions of fast-rise onset height decay indexes (n_{onset}) between our two twist groups if there are indeed systematic differences in their initiation mechanisms. The second panel of Figure 20 shows that there is no such difference, and the

same is true if we instead consider the average decay index between 42 and 105 Mm. This may be because of the limitations to our decay index estimates described in the previous section or because our sample is too small to detect a slight difference. Interestingly, Liu (2008) finds there to be no significant difference between the average decay indexes of kink and torus instability events, in contrast to the MHD simulations, and limitations to the PFSS modeling are also cited as a possible reason for this discrepancy. The fact that we find no difference in the decay indexes between events with and without apparent twisting motions therefore does not preclude differences in their initiation mechanisms. Moreover, we do not expect that all events in the twisted sample are initiated by the kink instability–most probably are not. Rather, we suggest simply that the likelihood is greater than for events without apparent twisting motions, which might explain the difference in onset height distributions. It may also be that more highly twisted filaments are likelier to facilitate a reconnection process at some point during their slow-rise phases before the torus instability threshold is reached.

The velocities plotted in the three rightmost panels of Figure 20 also tell an interesting story. We see from the middle panel that events with and without apparent twisting motions have no general differences in their slow-rise velocities. If, as we hypothesize, the twisting motions indicate greater helicity on average, then this similarity suggests that the flux rope helicity upon eruption is largely decoupled from the slow-rise velocity. This constraint is useful for modeling efforts, and it might lead one to speculate that there is a comparative homogeneity in the slow-rise mechanisms across events with disparate fast-rise mechanisms. As with the onset heights, velocity and acceleration differences emerge between the twist groups during the fast rise phase. We find that events with apparent twisting motions compared to those without have final speeds in our kinematics study that are 1.3× faster and CME speeds across the entire catalog that are 1.2× faster on average. While these enhancements are not very large, the cumulative distributions in Figure 20 indicate that the differences are statistically significant, with $A_k^2 = 1.9$ & $p = 0.05$ for the AIA speeds and $A_k^2 = 3.4$ & $p = 0.01$ for the CME speeds. This suggests that flux rope helicity may be positively correlated with CME speed, though a quantitative measure of helicity is needed to make this claim.

Two previous studies are particularly relevant to this possibility. Sung *et al.* (2009) found a positive correlation between the square of the initial CME speed and the magnetic helicity per unit length of the corresponding magnetic clouds at 1 AU for 34 events. Park *et al.* (2012) examined the average helicity injection ($\dot{H}$) of CME-producing active regions for a few days leading up to 47 eruptions using Michelson Doppler Imager (MDI) magnetograms and found a positive correlation between $\dot{H}$ and CME speed. This result is consistent with our finding, though it relates specifically to active region CMEs, while we find roughly the same enhancement across all filament types. However, when divided by type, our result remains statistically significant only for QS and PC events ($A_k^2 = 3.2$ & $p = 0.02$), for which there are over twice as many events compared the AR and IP sample ($A_k^2 = -0.12$ & $p = 0.39$). We also note from §3.4 that confined eruptions are significantly less likely to exhibit twisting motions (44% vs. 60% for the general population), implying lesser helicity on average. Confined events are often arrested by the overlying field because there is insufficient energy released to push through, and the fact that we find significantly lower rates of apparent twisting motions in these eruptions suggests, albeit somewhat tenuously, that we are reasonable in considering the twisted sample to be generally more energetic.

5.3. Future Work

A recently-submitted paper by Su *et al.* (2015) presents detailed modeling and observations for one of the polar crown events in our sample, which includes a more careful estimate of the decay index that employs STEREO observations to better constrain the location of the filament. This study implicates the torus instability as the driving mechanism through a comparison of the decay index to our fast-rise onset height. Reeves, McCauley, and Tian (2015) present a related study on a prominence eruption observed by the Interface Region Imaging Spectrograph (IRIS) that includes a comparison of the eruption kinematics to brightenings observed by both IRIS and AIA, which suggest that reconnection below the prominence triggered the fast-rise phase. The techniques employed by these works can be readily applied to our kinematics sample to estimate relative frequencies of the fast-rise onset mechanisms. The suggestive relationship between apparent twisting motions and CME speed can also be explored by quantifying the twist or overall helicity in quiescent filaments. This might be done using helicity injection measurements similar to that of Park *et al.* (2012) applied to HMI observations of events in the catalog observed on the disk or west limb, though the low flux densities in quiet sun regions may preclude reliable measurements. Alternatively, observations of untwisting motions similar to those presented by Yan *et al.* (2014) might be used to measure the extent to which filaments are twisted and then to compare with CME speed measurements.

6. Conclusion

This paper details the first statistical study of prominence eruptions observed by the Atmospheric Imaging Assembly (AIA) aboard the Solar Dynamics Observatory (SDO). An online catalog containing 904 eruptions was developed, listing several properties for each event that are intended to aid the community in identifying eruptions for future work (§2). Filaments are typed based on environment (active region (AR), intermediate (IP), quiescent (QS), or polar crown (PC)) along with the extent to which they erupt (full, partial, or confined), and comparisons between the type groups are made throughout (§3.1). A sample of 106 limb events was drawn from the catalog for a kinematics study that characterizes the distinct slow- and fast-rise phases often exhibited by prominence eruptions (§4). Our main results are summarized below:

1. Symmetric eruptions are found to be somewhat more common than asymmetric (48% vs. 38%), and symmetric events are 1.5× more likely to be full eruptions due to enhanced mass draining and detachments in asymmetric events (§3.2). Relatively few eruptions exhibit non-radial (12%) and sideways (11%) trajectories. Sideways trajectories are more commonly found in AR and IP events, which are likelier to be deflected strongly away from ARs. Sideways events are also more frequently confined or partial eruptions, likely because of interactions with neighboring structures that may arrest the eruption or facilitate additional draining (§3.3).
2. Vertical threads, perpendicular to the filament spines, are observed for 58% of events, which is interesting given their perplexing nature. The fraction of events with vertical threads by type scales with the characteristic sizes of the four types, with 11% for AR and 74% for PC eruptions. We note that vertical threads appear in ARs only for particularly large filaments, often in decaying active regions with well-separate polarities or at the boundary of what might instead be considered an intermediate filament (§3.6). Coronal cavities are also found most frequently in PC events, as expected. Overall, cavities are

absent in 49% of limb events, present in 34%, and become visible during the eruptions in 17% (§3.7).

3. 72% of our filament eruptions are associated with white-light CMEs observed by LASCO, and similar rates are found for each of the filament types. The CME speeds associated with AR and IP events are generally faster than those associated with QS and PC events by a factor of 1.3. IP-CMEs tend to be 1.1× faster than AR-CMEs, but this difference is not statistically significant (§3.8).
4. 106 limb events were selected from the catalog for a kinematics study, including 59 QS, 31 PC, 11 IP, and 6 AR prominence eruptions. Height-time plots were constructed for each event using 304 Å observations, and the Canny edge detection algorithm was used to extract individual height measurements (§4.1). A majority (74%) of the rise profiles are well-fit by an approximation introduced by Cheng *et al.* (2013), which combines a linear equation to treat the slow-rise phase and an exponential to treat the fast-rise. The onset of the fast-rise phase is defined as the point at which the exponential component of the curve equals the linear (§4.2). We also illustrate that apparent rise and fall velocities approaching 1 km s^{-1} can be observed due to solar rotation alone (§4.3).
5. The average values for the radial onset height ($h_{\rm onset}$), relative onset height ($\Delta h_{\rm onset}$), and slow-rise ($\Delta t_{\rm slow-rise}$) phase duration are 83 Mm, 29 Mm, and 4.4 hours, respectively. As expected, the lowest heights and shortest slow-rise phases are found for AR eruptions, and the largest heights and longest slow-rise phases are found for PC eruptions (§4.4.1). The average values for the slow-rise velocity ($v_{\rm slow-rise}$), maximum FOV velocity ($v_{\rm fov-max}$), and velocity at 500″ above the limb ($v_{500''}$) are 2.1, 106, and 183 km s^{-1}, respectively. The average onset acceleration ($a_{\rm onset}$), maximum FOV acceleration ($a_{\rm fov-max}$), and acceleration at 500″ ($a_{500''}$) are 1.9, 111, and 199 m s^{-2}, respectively. As with CME speed, we find that IP events are generally the fastest of the four types (§4.4.2). See Table 4 for the full list of statistical parameters and Table 5 for type comparisons.
6. The kinematics parameter distributions are best described by lognormal probability distributions similar to that of CME speeds, indicating that this pattern emerges in the low-corona (§4.4). An exception to this is the slow-rise phase velocity distribution for PC and possibly AR eruptions, which follow Gaussian distributions that shift to log-normality during the fast-rise phase. This may suggest a uniformity in the slow-rise process for PC and possibly AR filament eruptions compared to their QS and IP counterparts, whose more varied environments and size scales may provide more diverse influences (§4.4.2).
7. We find a positive correlation between latitude and fast-rise onset height, with correlation coefficients (r) of 0.30 and 0.43 for the radial and relative onset heights, respectively. A corresponding correlation between latitude and slow-rise phase duration is also found ($r = 0.50$). This is a global effect that diminishes if the eruptions are binned into latitude groups and is therefore likely to be a product of the global magnetic field. We interpret these correlations in terms of the decay index of the vertical magnetic field strength, which we find to exhibit a negative correlation with latitude using average decay indexes obtained from PFSS extrapolations between heights of 42 and 105 Mm. High-latitude events thus tend to have larger onset heights and longer slow-rise phases because they tend to have smaller decay indexes at a given height. We also find that the distribution of decay indexes at the onset of the fast-rise phase spans the full range of theoretical torus instability or loss of confinement critical thresholds (∼1–2), with an average value (1.1) consistent with the straight current channel approximation. A number of events

also exhibit critical decay indexes of < 1.0, indicating initiation by other means, such as reconnection or the kink instability (§5.1).

8. A majority of events (60%) exhibit apparent twisting motions, and IP filaments have the highest rate (68%). This includes several types of twist, of which untwisting motions seen in filament legs in the latter stages of an eruption are most common. We hypothesize that events with twisting motions have greater helicity on average, which is important to our interpretation of the relationships found between twist and eruption kinematics (see below). Confined eruptions exhibit twisting motions at a much lower rate (44%), which we interpret as a consequence of their comparatively limited magnetic energy (§3.4). A small fraction of events exhibit writhing motions suggestive of the kink instability (16%), but half of these are labeled as ambiguous. As expected, writhed events are much more likely to be partial or confined than the general population (§3.5).
9. Statistically significant differences are found between events that exhibit signs of twist and those that do not. Twisted events transition into their fast-rise phases at lower heights and have faster low-corona speeds, which might reflect different populations of fast-rise onset mechanisms that preferentially affect more or less twisted flux ropes. We also find that events with apparent twisting motions have faster coronagraph CME speeds by a factor of 1.2 across all events in the catalog. Though not very large, this difference is statistically significant ($p = 0.01$). Park *et al.* (2012) showed that helicity injection is positively correlated with CME speed for AR events, and our results indicate the same relationship for filament eruptions of all types. We also find that there is no difference in slow-rise speed for events with and without apparent twisting motions, which may imply that the flux rope helicity upon eruption is largely decoupled from the slow-rise mechanism and that there may be a comparative homogeneity in the slow-rise mechanisms across events with disparate fast-rise mechanisms (§5.2).

Acknowledgments Support for this work was provided by the National Aeronautics and Space Administration (NASA) through grant NNX12AI30G to the Smithsonian Astrophysical Observatory (SAO), by the National Science Foundation (NSF) through grant AGS1263241 for the solar physics Research Experiences for Undergraduates (REU) program at SAO, and by the Lockheed-Martin Solar and Astrophysics Laboratory (LMSAL) through contract SP02H1701R to SAO for support of the AIA. Additional support was provided by the National Science Foundation of China (NSFC) through grants No. 11333009, 11173062, 11473071, and J1210039, along with the Youth Fund of Jiangsu through grant No. BK20141043. The SDO is a NASA satellite, and the AIA instrument team is led by LMSAL. We gratefully acknowledge the anonymous referee for their constructive comments. P.I.M. thanks Sarah Gibson for her FORWARD tutorial, which facilitated our decay index analyses. We also thank the observers who contributed filament eruptions to the HEK: Anna Malanushenko, Nariaki Nitta, Wei Liu, Karel Schrijver, Mark Cheung, Ryan Timmons, Thomas Berger, Marc Derosa, Ralph Seguin, Paul Higgins, Juan Martínez-Skyora, Alberto Sainz-Dalda, Gregory Slater, and Neil Hurlburt.

References

Alexander, D., Metcalf, T.R., Nitta, N.V.: 2002, Fast acceleration of a CME-related X-ray structure in the low solar corona. *Geophys. Res. Lett.* **29**, 1403. DOI. ADS.

Amari, T., Aly, J.-J., Mikic, Z., Linker, J.: 2010, Coronal Mass Ejection Initiation: On the Nature of the Flux Cancellation Model. *Astrophys. J. Lett.* **717**, L26. DOI. ADS.

Antiochos, S.K., DeVore, C.R., Klimchuk, J.A.: 1999, A Model for Solar Coronal Mass Ejections. *Astrophys. J.* **510**, 485. DOI. ADS.

Aulanier, G., Török, T., Démoulin, P., DeLuca, E.E.: 2010, Formation of Torus-Unstable Flux Ropes and Electric Currents in Erupting Sigmoids. *Astrophys. J.* **708**, 314. DOI. ADS.

Bateman, G.: 1978, *MHD instabilities*. ADS.

Bein, B.M., Berkebile-Stoiser, S., Veronig, A.M., Temmer, M., Muhr, N., Kienreich, I., Utz, D., Vršnak, B.: 2011, Impulsive Acceleration of Coronal Mass Ejections. I. Statistics and Coronal Mass Ejection Source Region Characteristics. *Astrophys. J.* **738**, 191. DOI. ADS.

Berger, T., Testa, P., Hillier, A., Boerner, P., Low, B.C., Shibata, K., Schrijver, C., Tarbell, T., Title, A.: 2011, Magneto-thermal convection in solar prominences. *Nature* **472**, 197. DOI. ADS.

Brueckner, G.E., Howard, R.A., Koomen, M.J., Korendyke, C.M., Michels, D.J., Moses, J.D., Socker, D.G., Dere, K.P., Lamy, P.L., Llebaria, A., Bout, M.V., Schwenn, R., Simnett, G.M., Bedford, D.K., Eyles, C.J.: 1995, The Large Angle Spectroscopic Coronagraph (LASCO). *Solar Phys.* **162**, 357. DOI. ADS.

Canny, J.: 1986, A computational approach to edge detection. *IEEE Trans. Pattern Anal. Mach. Intell.* **8**(6), 679. DOI.

Chae, J.: 2010, Dynamics of Vertical Threads and Descending Knots in a Hedgerow Prominence. *Astrophys. J.* **714**, 618. DOI. ADS.

Chen, B., Bastian, T.S., Gary, D.E.: 2014, Direct Evidence of an Eruptive, Filament-hosting Magnetic Flux Rope Leading to a Fast Solar Coronal Mass Ejection. *Astrophys. J.* **794**, 149. DOI. ADS.

Chen, P.F., Shibata, K.: 2000, An Emerging Flux Trigger Mechanism for Coronal Mass Ejections. *Astrophys. J.* **545**, 524. DOI. ADS.

Cheng, X., Zhang, J., Ding, M.D., Olmedo, O., Sun, X.D., Guo, Y., Liu, Y.: 2013, Investigating Two Successive Flux Rope Eruptions in a Solar Active Region. *Astrophys. J. Lett.* **769**, L25. DOI. ADS.

Chifor, C., Mason, H.E., Tripathi, D., Isobe, H., Asai, A.: 2006, The early phases of a solar prominence eruption and associated flare: a multi-wavelength analysis. *Astron. Astrophys.* **458**, 965. DOI. ADS.

Chifu, I., Inhester, B., Mierla, M., Chifu, V., Wiegelmann, T.: 2012, First 4D Reconstruction of an Eruptive Prominence Using Three Simultaneous View Directions. *Solar Phys.* **281**, 121. DOI. ADS.

D'Agostino, R.B., Stephens, M.A. (eds.): 1986, *Goodness-of-fit techniques*, Marcel Dekker, Inc., New York, NY, USA. ISBN 0-824-77487-6.

Démoulin, P., Aulanier, G.: 2010, Criteria for Flux Rope Eruption: Non-equilibrium Versus Torus Instability. *Astrophys. J.* **718**, 1388. DOI. ADS.

Domingo, V., Fleck, B., Poland, A.I.: 1995, The SOHO Mission: an Overview. *Solar Phys.* **162**, 1. DOI. ADS.

Engvold, O.: 2015, Description and Classification of Prominences. In: Vial, J.-C., Engvold, O. (eds.) *Astrophysics and Space Science Library*, *Astrophysics and Space Science Library* **415**, 31. DOI. ADS.

Fan, Y.: 2012, Thermal Signatures of Tether-cutting Reconnections in Pre-eruption Coronal Flux Ropes: Hot Central Voids in Coronal Cavities. *Astrophys. J.* **758**, 60. DOI. ADS.

Fan, Y.: 2015, MHD Equilibria and Triggers for Prominence Eruption. In: Vial, J.-C., Engvold, O. (eds.) *Astrophysics and Space Science Library*, *Astrophysics and Space Science Library* **415**, 297. DOI. ADS.

Fan, Y., Gibson, S.E.: 2007, Onset of Coronal Mass Ejections Due to Loss of Confinement of Coronal Flux Ropes. *Astrophys. J.* **668**, 1232. DOI. ADS.

Filippov, B.P.: 2013, Height of a solar filament before eruption. *Astronomy Reports* **57**, 778. DOI. ADS.

Filippov, B.P., Den, O.G.: 2000, Prominence Height and Vertical Gradient in Magnetic Field. *Astronomy Letters* **26**, 322. DOI. ADS.

Filippov, B.P., Den, O.G.: 2001, A critical height of quiescent prominences before eruption. *J. Geophys. Res.* **106**, 25177. DOI. ADS.

Forland, B.C., Gibson, S.E., Dove, J.B., Rachmeler, L.A., Fan, Y.: 2013, Coronal Cavity Survey: Morphological Clues to Eruptive Magnetic Topologies. *Solar Phys.* **288**, 603. DOI. ADS.

Foullon, C., Verwichte, E.: 2006, Automated Detection of EUV Prominences. *Solar Phys.* **234**, 135. DOI. ADS.

Fuller, J., Gibson, S.E.: 2009, A Survey of Coronal Cavity Density Profiles. *Astrophys. J.* **700**, 1205. DOI. ADS.

Gibson, S.: 2015, Coronal Cavities: Observations and Implications for the Magnetic Environment of Prominences. In: Vial, J.-C., Engvold, O. (eds.) *Astrophysics and Space Science Library*, *Astrophysics and*

Space Science Library **415**, 323. DOI. ADS.

Gibson, S.E., Fan, Y.: 2006, Coronal prominence structure and dynamics: A magnetic flux rope interpretation. *Journal of Geophysical Research (Space Physics)* **111**(A10), 12103. DOI. ADS.

Gibson, S.E., Kucera, T.A., Casini, R., Dove, J., Forland, B., Judge, P., Rachmeler, L.: 2014, *FORWARD: Forward modeling of coronal observables*, Astrophysics Source Code Library. ADS.

Gilbert, H.R., Alexander, D., Liu, R.: 2007, Filament Kinking and Its Implications for Eruption and Re-formation. *Solar Phys.* **245**, 287. DOI. ADS.

Gilbert, H.R., Holzer, T.E., Burkepile, J.T., Hundhausen, A.J.: 2000, Active and Eruptive Prominences and Their Relationship to Coronal Mass Ejections. *Astrophys. J.* **537**, 503. DOI. ADS.

Goff, C.P., van Driel-Gesztelyi, L., Harra, L.K., Matthews, S.A., Mandrini, C.H.: 2005, A slow coronal mass ejection with rising X-ray source. *Astron. Astrophys.* **434**, 761. DOI. ADS.

Gopalswamy, N.: 2015, The Dynamics of Eruptive Prominences. In: Vial, J.-C., Engvold, O. (eds.) *Astrophysics and Space Science Library*, *Astrophysics and Space Science Library* **415**, 381. DOI. ADS.

Gopalswamy, N., Shimojo, M., Lu, W., Yashiro, S., Shibasaki, K., Howard, R.A.: 2003, Prominence Eruptions and Coronal Mass Ejection: A Statistical Study Using Microwave Observations. *Astrophys. J.* **586**, 562. DOI. ADS.

Gui, B., Shen, C., Wang, Y., Ye, P., Liu, J., Wang, S., Zhao, X.: 2011, Quantitative Analysis of CME Deflections in the Corona. *Solar Phys.* **271**, 111. DOI. ADS.

Howard, R.A., Moses, J.D., Vourlidas, A., Newmark, J.S., Socker, D.G., Plunkett, S.P., Korendyke, C.M., Cook, J.W., Hurley, A., Davila, J.M., Thompson, W.T., St Cyr, O.C., Mentzell, E., Mehalick, K., Lemen, J.R., Wuelser, J.P., Duncan, D.W., Tarbell, T.D., Wolfson, C.J., Moore, A., Harrison, R.A., Waltham, N.R., Lang, J., Davis, C.J., Eyles, C.J., Mapson-Menard, H., Simnett, G.M., Halain, J.P., Defise, J.M., Mazy, E., Rochus, P., Mercier, R., Ravet, M.F., Delmotte, F., Auchere, F., Delaboudiniere, J.P., Bothmer, V., Deutsch, W., Wang, D., Rich, N., Cooper, S., Stephens, V., Maahs, G., Baugh, R., McMullin, D., Carter, T.: 2008, Sun Earth Connection Coronal and Heliospheric Investigation (SECCHI). *Space Sci. Rev.* **136**, 67. DOI. ADS.

Hundhausen, A.: 1999, Coronal Mass Ejections. In: Strong, K.T., Saba, J.L.R., Haisch, B.M., Schmelz, J.T. (eds.) *The many faces of the sun: a summary of the results from NASA's Solar Maximum Mission.*, 143. ADS.

Hurlburt, N., Cheung, M., Schrijver, C., Chang, L., Freeland, S., Green, S., Heck, C., Jaffey, A., Kobashi, A., Schiff, D., Serafin, J., Seguin, R., Slater, G., Somani, A., Timmons, R.: 2012, Heliophysics Event Knowledgebase for the Solar Dynamics Observatory (SDO) and Beyond. *Solar Phys.* **275**, 67. DOI. ADS.

Isobe, H., Tripathi, D., Asai, A., Jain, R.: 2007, Large-Amplitude Oscillation of an Erupting Filament as Seen in EUV, Hα, and Microwave Observations. *Solar Phys.* **246**, 89. DOI. ADS.

Joshi, A.D., Srivastava, N.: 2011, Kinematics of Two Eruptive Prominences Observed by EUVI/STEREO. *Astrophys. J.* **730**, 104. DOI. ADS.

Joshi, V., Srivastava, N.: 2007, On the study of kinematics of eruptive quiescent prominences observed in He 304 Å. *Bulletin of the Astronomical Society of India* **35**, 447. ADS.

Kay, C., Opher, M., Evans, R.M.: 2014, Global Trends of CME Deflections Based on CME and Solar Parameters. *ArXiv e-prints*. ADS.

Kliem, B., Török, T.: 2006, Torus Instability. *Physical Review Letters* **96**(25), 255002. DOI. ADS.

Koleva, K., Madjarska, M.S., Duchlev, P., Schrijver, C.J., Vial, J.-C., Buchlin, E., Dechev, M.: 2012, Kinematics and helicity evolution of a loop-like eruptive prominence. *Astron. Astrophys.* **540**, A127. DOI. ADS.

Kundu, M.R., White, S.M., Garaimov, V.I., Manoharan, P.K., Subramanian, P., Ananthakrishnan, S., Janardhan, P.: 2004, Radio Observations of Rapid Acceleration in a Slow Filament Eruption/Fast Coronal Mass Ejection Event. *Astrophys. J.* **607**, 530. DOI. ADS.

Labrosse, N., Schmieder, B., Heinzel, P., Watanabe, T.: 2011, EUV lines observed with EIS/Hinode in a solar prominence. *Astron. Astrophys.* **531**, A69. DOI. ADS.

Lemen, J.R., Title, A.M., Akin, D.J., Boerner, P.F., Chou, C., Drake, J.F., Duncan, D.W., Edwards, C.G., Friedlaender, F.M., Heyman, G.F., Hurlburt, N.E., Katz, N.L., Kushner, G.D., Levay, M., Lind-

gren, R.W., Mathur, D.P., McFeaters, E.L., Mitchell, S., Rehse, R.A., Schrijver, C.J., Springer, L.A., Stern, R.A., Tarbell, T.D., Wuelser, J.-P., Wolfson, C.J., Yanari, C., Bookbinder, J.A., Cheimets, P.N., Caldwell, D., Deluca, E.E., Gates, R., Golub, L., Park, S., Podgorski, W.A., Bush, R.I., Scherrer, P.H., Gummin, M.A., Smith, P., Auker, G., Jerram, P., Pool, P., Soufli, R., Windt, D.L., Beardsley, S., Clapp, M., Lang, J., Waltham, N.: 2012, The Atmospheric Imaging Assembly (AIA) on the Solar Dynamics Observatory (SDO). *Solar Phys.* **275**, 17. DOI. ADS.

Leroy, J.L., Bommier, V., Sahal-Brechot, S.: 1984, New data on the magnetic structure of quiescent prominences. *Astron. Astrophys.* **131**, 33. ADS.

Limpert, E., Stahel, W.A., Abbt, M.: 2001, Log-normal distributions across the sciences: Keys and clues. *BioScience* **51**(5), 341. http://www.stat.math.ethz.ch/~stahel/lognormal/bioscience.pdf.

Lin, J., Forbes, T.G.: 2000, Effects of reconnection on the coronal mass ejection process. *J. Geophys. Res.* **105**, 2375. DOI. ADS.

Lin, Y., Martin, S.F., Engvold, O.: 2008, Filament Substructures and their Interrelation. In: Howe, R., Komm, R.W., Balasubramaniam, K.S., Petrie, G.J.D. (eds.) *Subsurface and Atmospheric Influences on Solar Activity*, *Astronomical Society of the Pacific Conference Series* **383**, 235. ADS.

Liu, K., Wang, Y., Shen, C., Wang, S.: 2012a, Critical Height for the Destabilization of Solar Prominences: Statistical Results from STEREO Observations. *Astrophys. J.* **744**, 168. DOI. ADS.

Liu, R., Alexander, D., Gilbert, H.R.: 2009, Asymmetric Eruptive Filaments. *Astrophys. J.* **691**, 1079. DOI. ADS.

Liu, R., Kliem, B., Török, T., Liu, C., Titov, V.S., Lionello, R., Linker, J.A., Wang, H.: 2012b, Slow Rise and Partial Eruption of a Double-decker Filament. I. Observations and Interpretation. *Astrophys. J.* **756**, 59. DOI. ADS.

Liu, Y.: 2008, Magnetic Field Overlying Solar Eruption Regions and Kink and Torus Instabilities. *Astrophys. J. Lett.* **679**, L151. DOI. ADS.

Low, B.C., Hundhausen, J.R.: 1995, Magnetostatic structures of the solar corona. 2: The magnetic topology of quiescent prominences. *Astrophys. J.* **443**, 818. DOI. ADS.

Low, B.C., Berger, T., Casini, R., Liu, W.: 2012a, The Hydromagnetic Interior of a Solar Quiescent Prominence. I. Coupling between Force Balance and Steady Energy Transport. *Astrophys. J.* **755**, 34. DOI. ADS.

Low, B.C., Liu, W., Berger, T., Casini, R.: 2012b, The Hydromagnetic Interior of a Solar Quiescent Prominence. II. Magnetic Discontinuities and Cross-field Mass Transport. *Astrophys. J.* **757**, 21. DOI. ADS.

Lugaz, N.: 2015, Eruptive Prominences and Their Impact on the Earth and Our Life. In: Vial, J.-C., Engvold, O. (eds.) *Astrophysics and Space Science Library*, *Astrophysics and Space Science Library* **415**, 433. DOI. ADS.

Mackay, D.H.: 2015, Formation and Large-Scale Patterns of Filament Channels and Filaments. In: Vial, J.-C., Engvold, O. (eds.) *Astrophysics and Space Science Library*, *Astrophysics and Space Science Library* **415**, 355. DOI. ADS.

Mackay, D.H., Gaizauskas, V., Yeates, A.R.: 2008, Where Do Solar Filaments Form?: Consequences for Theoretical Models. *Solar Phys.* **248**, 51. DOI. ADS.

Makarov, V.I.: 1994, Global magnetic activity in 22-year solar cycles. *Solar Phys.* **150**, 359. DOI. ADS.

Makarov, V.I., Tavastsherna, K.S., Davydova, E.I., Sivaraman, K.R.: 1992, Variations of prominence heights in high latitude global magnetic neutral lines. *Byulletin Solnechnye Dannye Akademie Nauk SSSR* **3**, 90. ADS.

Maričić, D., Vršnak, B., Roša, D.: 2009, Relative Kinematics of the Leading Edge and the Prominence in Coronal Mass Ejections. *Solar Phys.* **260**, 177. DOI. ADS.

Markwardt, C.B.: 2009, Non-linear Least-squares Fitting in IDL with MPFIT. In: Bohlender, D.A., Durand, D., Dowler, P. (eds.) *Astronomical Data Analysis Software and Systems XVIII*, *Astronomical Society of the Pacific Conference Series* **411**, 251. ADS.

Martin, S.F.: 2003, Signs of helicity in solar prominences and related features. *Advances in Space Research* **32**, 1883. DOI. ADS.

Masson, S., McCauley, P., Golub, L., Reeves, K.K., DeLuca, E.E.: 2014, Dynamics of the Transition

Corona. *Astrophys. J.* **787**, 145. DOI. ADS.

McKillop, S., Miralles, M.P., Murphy, N.A., McCauley, P.: 2014, Rolling Motions During Solar Prominence Eruptions in Asymmetric Magnetic Environments. In: *American Astronomical Society Meeting Abstracts #224*, *American Astronomical Society Meeting Abstracts* **224**, #218.30. ADS.

Moon, Y.-J., Choe, G.S., Wang, H., Park, Y.D., Gopalswamy, N., Yang, G., Yashiro, S.: 2002, A Statistical Study of Two Classes of Coronal Mass Ejections. *Astrophys. J.* **581**, 694. DOI. ADS.

Munro, R.H., Gosling, J.T., Hildner, E., MacQueen, R.M., Poland, A.I., Ross, C.L.: 1979, The association of coronal mass ejection transients with other forms of solar activity. *Solar Phys.* **61**, 201. DOI. ADS.

Murphy, N.A., Miralles, M.P., Pope, C.L., Raymond, J.C., Winter, H.D., Reeves, K.K., Seaton, D.B., van Ballegooijen, A.A., Lin, J.: 2012, Asymmetric Magnetic Reconnection in Solar Flare and Coronal Mass Ejection Current Sheets. *Astrophys. J.* **751**, 56. DOI. ADS.

Paletou, F., López Ariste, A., Bommier, V., Semel, M.: 2001, Full-Stokes spectropolarimetry of solar prominences. *Astron. Astrophys.* **375**, L39. DOI. ADS.

Panasenco, O., Martin, S., Joshi, A.D., Srivastava, N.: 2011, Rolling motion in erupting prominences observed by STEREO. *Journal of Atmospheric and Solar-Terrestrial Physics* **73**, 1129. DOI. ADS.

Panasenco, O., Martin, S.F., Velli, M., Vourlidas, A.: 2013, Origins of Rolling, Twisting, and Non-radial Propagation of Eruptive Solar Events. *Solar Phys.* **287**, 391. DOI. ADS.

Parenti, S.: 2014, Solar Prominences: Observations. *Living Reviews in Solar Physics* **11**, 1. DOI. ADS.

Park, S.-H., Cho, K.-S., Bong, S.-C., Kumar, P., Chae, J., Liu, R., Wang, H.: 2012, The Occurrence and Speed of CMEs Related to Two Characteristic Evolution Patterns of Helicity Injection in Their Solar Source Regions. *Astrophys. J.* **750**, 48. DOI. ADS.

Pesnell, W.D., Thompson, B.J., Chamberlin, P.C.: 2012, The Solar Dynamics Observatory (SDO). *Solar Phys.* **275**, 3. DOI. ADS.

Reeves, K.K., McCauley, P.I., Tian, H.: 2015, Direct Observations of Magnetic Reconnection Outflow and CME Triggering in a Small Erupting Solar Prominence. *Astrophys. J.* **in press**.

Reeves, K.K., Linker, J.A., Mikić, Z., Forbes, T.G.: 2010, Current Sheet Energetics, Flare Emissions, and Energy Partition in a Simulated Solar Eruption. *Astrophys. J.* **721**, 1547. DOI. ADS.

Reeves, K.K., Gibson, S.E., Kucera, T.A., Hudson, H.S., Kano, R.: 2012, Thermal Properties of a Solar Coronal Cavity Observed with the X-Ray Telescope on Hinode. *Astrophys. J.* **746**, 146. DOI. ADS.

Régnier, S., Walsh, R.W., Alexander, C.E.: 2011, A new look at a polar crown cavity as observed by SDO/AIA. Structure and dynamics. *Astron. Astrophys.* **533**, L1. DOI. ADS.

Robbrecht, E., Berghmans, D.: 2004, Automated recognition of coronal mass ejections (CMEs) in near-real-time data. *Astron. Astrophys.* **425**, 1097. DOI. ADS.

Robbrecht, E., Berghmans, D., Van der Linden, R.A.M.: 2009, Automated LASCO CME Catalog for Solar Cycle 23: Are CMEs Scale Invariant? *Astrophys. J.* **691**, 1222. DOI. ADS.

Romano, P., Contarino, L., Zuccarello, F.: 2003, Eruption of a helically twisted prominence. *Solar Phys.* **214**, 313. DOI. ADS.

Savcheva, A.S., McKillop, S.C., McCauley, P.I., Hanson, E.M., DeLuca, E.E.: 2014, A New Sigmoid Catalog from Hinode and the Solar Dynamics Observatory: Statistical Properties and Evolutionary Histories. *Solar Phys.* **289**, 3297. DOI. ADS.

Scherrer, P.H., Schou, J., Bush, R.I., Kosovichev, A.G., Bogart, R.S., Hoeksema, J.T., Liu, Y., Duvall, T.L., Zhao, J., Title, A.M., Schrijver, C.J., Tarbell, T.D., Tomczyk, S.: 2012, The Helioseismic and Magnetic Imager (HMI) Investigation for the Solar Dynamics Observatory (SDO). *Solar Phys.* **275**, 207. DOI. ADS.

Scholz, F.W., Stephens, M.A.: 1987, K-sample anderson–darling tests. *Journal of the American Statistical Association* **82**(399), 918.

Schrijver, C.J., De Rosa, M.L.: 2003, Photospheric and heliospheric magnetic fields. *Solar Phys.* **212**, 165. DOI. ADS.

Schrijver, C.J., Elmore, C., Kliem, B., Török, T., Title, A.M.: 2008, Observations and Modeling of the Early Acceleration Phase of Erupting Filaments Involved in Coronal Mass Ejections. *Astrophys. J.* **674**, 586. DOI. ADS.

Sheeley, N.R. Jr., Michels, D.J., Howard, R.A., Koomen, M.J.: 1980, Initial observations with the

SOLWIND coronagraph. *Astrophys. J. Lett.* **237**, L99. DOI. ADS.

Simnett, G.M.: 2000, The relationship between prominence eruptions and coronal mass ejections. *Journal of Atmospheric and Solar-Terrestrial Physics* **62**, 1479. DOI. ADS.

Sterling, A.C., Moore, R.L.: 2004, Evidence for Gradual External Reconnection before Explosive Eruption of a Solar Filament. *Astrophys. J.* **602**, 1024. DOI. ADS.

Sterling, A.C., Moore, R.L.: 2005, Slow-Rise and Fast-Rise Phases of an Erupting Solar Filament, and Flare Emission Onset. *Astrophys. J.* **630**, 1148. DOI. ADS.

Sterling, A.C., Harra, L.K., Moore, R.L.: 2007, New Evidence for the Role of Emerging Flux in a Solar Filament's Slow Rise Preceding Its CME-producing Fast Eruption. *Astrophys. J.* **669**, 1359. DOI. ADS.

Sterling, A.C., Moore, R.L., Freeland, S.L.: 2011, Insights into Filament Eruption Onset from Solar Dynamics Observatory Observations. *Astrophys. J. Lett.* **731**, L3. DOI. ADS.

Sterling, A.C., Moore, R.L., Berger, T.E., Bobra, M., Davis, J.M., Jibben, P., Kano, R., Lundquist, L.L., Myers, D., Narukage, N., Sakao, T., Shibasaki, K., Shine, R.A., Tarbell, T.D., Weber, M.: 2007, Hinode Observations of the Onset Stage of a Solar Filament Eruption. *Pub. Astron. Soc. Japan* **59**, 823. DOI. ADS.

Su, Y., van Ballegooijen, A.: 2012, Observations and Magnetic Field Modeling of a Solar Polar Crown Prominence. *Astrophys. J.* **757**, 168. DOI. ADS.

Su, Y., van Ballegooijen, A.: 2013, Rotating Motions and Modeling of the Erupting Solar Polar-crown Prominence on 2010 December 6. *Astrophys. J.* **764**, 91. DOI. ADS.

Su, Y., Lu, M., van Ballegooijen, A.: 2012, Structure and Dynamics of Quiescent Prominence Eruptions. In: Golub, L., De Moortel, I., Shimizu, T. (eds.) *Fifth Hinode Science Meeting*, *Astronomical Society of the Pacific Conference Series* **456**, 165. ADS.

Su, Y., van Ballegooijen, A., McCauley, P.I., Haisheng, J., Reeves, K.K., E., D.: 2015, Magnetic Structure and Dynamics of the Erupting Solar Polar Crown Prominence on 2012 March 12. *Astrophys. J.* **submitted**.

Sung, S.-K., Marubashi, K., Cho, K.-S., Kim, Y.-H., Kim, K.-H., Chae, J., Moon, Y.-J., Kim, I.-H.: 2009, A Comparison of the Initial Speed of Coronal Mass Ejections with the Magnetic Flux and Magnetic Helicity of Magnetic Clouds. *Astrophys. J.* **699**, 298. DOI. ADS.

Tandberg-Hanssen, E.: 1998, The History of Solar Prominence Research (Review). In: Webb, D.F., Schmieder, B., Rust, D.M. (eds.) *IAU Colloq. 167: New Perspectives on Solar Prominences*, *Astronomical Society of the Pacific Conference Series* **150**, 11. ADS.

Thompson, W.T.: 2013, Alternating Twist Along an Erupting Prominence. *Solar Phys.* **283**, 489. DOI. ADS.

Török, T., Kliem, B.: 2005, Confined and Ejective Eruptions of Kink-unstable Flux Ropes. *Astrophys. J. Lett.* **630**, L97. DOI. ADS.

Török, T., Berger, M.A., Kliem, B.: 2010, The writhe of helical structures in the solar corona. *Astron. Astrophys.* **516**, A49. DOI. ADS.

Tripathi, D., Isobe, H., Mason, H.E.: 2006, On the propagation of brightening after filament/prominence eruptions, as seen by SoHO-EIT. *Astron. Astrophys.* **453**, 1111. DOI. ADS.

Tripathi, D., Reeves, K.K., Gibson, S.E., Srivastava, A., Joshi, N.C.: 2013, SDO/AIA Observations of a Partially Erupting Prominence. *Astrophys. J.* **778**, 142. DOI. ADS.

Tziotziou, K., Moraitis, K., Georgoulis, M.K., Archontis, V.: 2014, Validation of the magnetic energy vs. helicity scaling in solar magnetic structures. *Astron. Astrophys.* **570**, L1. DOI. ADS.

van Ballegooijen, A.A., Cranmer, S.R.: 2010, Tangled Magnetic Fields in Solar Prominences. *Astrophys. J.* **711**, 164. DOI. ADS.

van Ballegooijen, A.A., Martens, P.C.H.: 1989, Formation and eruption of solar prominences. *Astrophys. J.* **343**, 971. DOI. ADS.

van Tend, W., Kuperus, M.: 1978, The development of coronal electric current systems in active regions and their relation to filaments and flares. *Solar Phys.* **59**, 115. DOI. ADS.

Vial, J.-C., Engvold, O. (eds.): 2015, *Solar Prominences*, *Astrophysics and Space Science Library* **415**. DOI. ADS.

Wang, Y., Cao, H., Chen, J., Zhang, T., Yu, S., Zheng, H., Shen, C., Zhang, J., Wang, S.: 2010, Solar Limb

Prominence Catcher and Tracker (SLIPCAT): An Automated System and its Preliminary Statistical Results. *Astrophys. J.* **717**, 973. DOI. ADS.

Webb, D.F.: 2015, Eruptive Prominences and Their Association with Coronal Mass Ejections. In: Vial, J.-C., Engvold, O. (eds.) *Astrophysics and Space Science Library*, *Astrophysics and Space Science Library* **415**, 411. DOI. ADS.

Williams, D.R., Baker, D., van Driel-Gesztelyi, L.: 2013, Mass Estimates of Rapidly Moving Prominence Material from High-cadence EUV Images. *Astrophys. J.* **764**, 165. DOI. ADS.

Williams, D.R., Török, T., Démoulin, P., van Driel-Gesztelyi, L., Kliem, B.: 2005, Eruption of a Kink-unstable Filament in NOAA Active Region 10696. *Astrophys. J. Lett.* **628**, L163. DOI. ADS.

Wuelser, J.-P., Lemen, J.R., Tarbell, T.D., Wolfson, C.J., Cannon, J.C., Carpenter, B.A., Duncan, D.W., Gradwohl, G.S., Meyer, S.B., Moore, A.S., Navarro, R.L., Pearson, J.D., Rossi, G.R., Springer, L.A., Howard, R.A., Moses, J.D., Newmark, J.S., Delaboudiniere, J.-P., Artzner, G.E., Auchere, F., Bougnet, M., Bouyries, P., Bridou, F., Clotaire, J.-Y., Colas, G., Delmotte, F., Jerome, A., Lamare, M., Mercier, R., Mullot, M., Ravet, M.-F., Song, X., Bothmer, V., Deutsch, W.: 2004, EUVI: the STEREO-SECCHI extreme ultraviolet imager. In: Fineschi, S., Gummin, M.A. (eds.) *Telescopes and Instrumentation for Solar Astrophysics*, *Society of Photo-Optical Instrumentation Engineers (SPIE) Conference Series* **5171**, 111. DOI. ADS.

Yan, X.L., Xue, Z.K., Liu, J.H., Ma, L., Kong, D.F., Qu, Z.Q., Li, Z.: 2014, Kink Instability Evidenced by Analyzing the Leg Rotation of a Filament. *Astrophys. J.* **782**, 67. DOI. ADS.

Yurchyshyn, V., Yashiro, S., Abramenko, V., Wang, H., Gopalswamy, N.: 2005, Statistical Distributions of Speeds of Coronal Mass Ejections. *Astrophys. J.* **619**, 599. DOI. ADS.

Zhang, J., Dere, K.P.: 2006, A Statistical Study of Main and Residual Accelerations of Coronal Mass Ejections. *Astrophys. J.* **649**, 1100. DOI. ADS.